ELSEVIER

Contents lists available at ScienceDirect

Ocean Engineering

journal homepage: www.elsevier.com/locate/oceaneng



Research paper

Operability analysis for collaborative caisson towing using multiple towlines in shallow waters with complex seabed topography

Zongyuan Yang, Zhengru Ren*

Institute for Ocean Engineering, Shenzhen International Graduate School, Tsinghua University, Tsinghua Campus, University Town, Shenzhen 518055, China

ARTICLE INFO

Keywords: Caisson Towing in shallow waters CDPR Passable region Operability analysis

ABSTRACT

Caissons, typically transported via towing, face significant challenges in shallow waters, including limited passability, grounding risk, and restricted maneuverability. Conventional wet- and dry-towing methods have proven inadequate due to vessel constraints and depth limitations. Instead, the present study proposes a multi-towline collaborative towing method based on a framework of cable-driven parallel robots to enhance operational flexibility. To consider complex shallow-water seabed topography and prevent caissons from hitting the seabed, an operability analysis framework can be used to evaluate environmental conditions (ECs) through a discretized bathymetry map, converting elevation data into seabed wedge modules. This probabilistic methodology integrates potential flow theory results validated by computational fluid dynamics with time-domain multi-body simulations for extreme value analysis. A distance-based criterion is employed to assess caisson passability under specific ECs. Parametric analysis across varying water depths, slopes, and aspects is used to establish characteristic distances and a data-driven approach employed to explore any nonlinear relationships, enabling passable region determination. The results demonstrate that seabed slope and aspect significantly influence caisson hydrodynamics, with water depth, slope, and aspect collectively determining passable regions.

1. Introduction

Caissons are widely utilized in the construction of various offshore and coastal structures in shallow waters, including harbor walls (Hendry, 1983), breakwaters (Ye et al., 2021; Zhou and Ye, 2022), and cross-sea bridges (Wei et al., 2022; Qiu et al., 2023). Typically, caissons lack self-propulsion capabilities and are transported to the designated location by being towed by tugboats or carried by semi-submersible vessels.

Early research on caisson towing focused on conventional dry towing by semi-submersible vessels and wet towing by tugboats. For numerical simulations, potential flow theory is commonly employed and the towing effect considered through the application of a current in the opposite direction that is equal to the towing speed (Kang and Kim, 2014; Heo and Park, 2016). Hydrodynamics in shallow waters are very complicated (Gu et al., 2024b; Xing and Chen, 2017). The hydrodynamic response caused by cable breakage during towing has been investigated in previous research (Gu et al., 2024a). Slip forces induced by inertia and gravity have also been explored for caisson towing by tugboats and semi-submersible vessels in various wind-wave conditions (Kang and Kim, 2014; Alam et al., 2025; Li et al., 2016). The influence of towing speed has also been studied (Park et al., 2018).

However, towing caissons in shallow waters poses certain challenges. From 2000 to 2020, grounding incidents accounted for 7% of maritime accidents in China (Deng et al., 2021). Among these, floating structures and small vessels with a total length of less than 50 meters exhibited a grounding frequency of 79% (Pilatis et al., 2024). Notably, the primary dimensions of caissons fall within this size range. First, water depth limits passability. Second, obstacles resulting from the complex seabed topography such as underlying rocks and the rocky sides of coastlines result in a higher likelihood of grounding incidents. Third, caisson maneuverability affects safety and efficiency. There have been a number of incidents where a towed object has failed to avoid obstacles during towage due to maneuvering limitations and the massive inertia of tugboats (Transportation Safety Board of Canada, 2008). Moreover, the risk of grounding accidents caused by ineffective tugboat course-keeping remains high (National Transportation Safety Board Marine Accident Brief, 2013). Wave-induced motion increases the magnitude of caisson motion and the risk of hitting the seabed.

Conventional wet towing by tugboats is constrained by their maneuverability, hindering caissons' effective obstacle avoidance and increasing grounding risk. According to the China Classification Society,

E-mail addresses: yang-zy22@mails.tsinghua.edu.cn (Z. Yang), zhengru.ren@sz.tsinghua.edu.cn (Z. Ren).

^{*} Corresponding author.

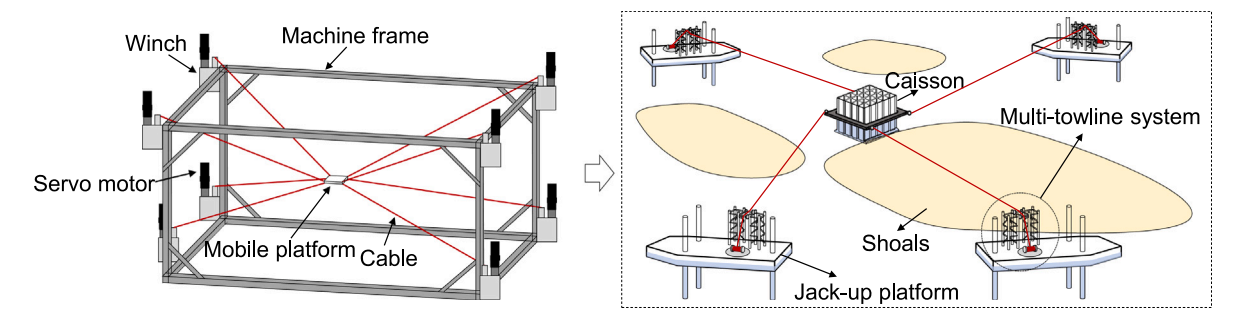


Fig. 1. The composition of the CDPR (left) and the MTCT mechanism (right).

tugboats should stay far away from shallow water regions (China Classification Society, 2011). Alternatively, dry towing uses a large semi-submersible vessel, typically with a summer draft exceeding 6.09 m (Boskails, 2018). Their sizeable dimensions require a certain water depth for submersion. Consequently, conventional towing methods are unsuitable for shallow water caisson towing, necessitating the establishment of a novel towing method suitable for shallow waters with complex seabed topographies.

Cable-driven parallel robots (CDPRs) employ multiple parallel-arranged flexible cables to realize the precise motion control of a mobile platform and are widely applied in fields such as offshore lifting operations (Zhao et al., 2024; Ren et al., 2021; Sun et al., 2023; Chen et al., 2024; Ma et al., 2025) and radio telescopes (Nan et al., 2011). Similar to the framework of a CDPR, a multi-towline collaborative towing (MTCT) mechanism for caissons is proposed here (see Fig. 1). Such a mechanism will effectively improve the maneuverability and flexibility of caisson towing, as well as reduce the required water depth. The details are described below in Section 2.1.

Appropriate sea states must be selected to ensure that caissons do not hit the seabed during towing, resulting in a lower risk of structural damage (Zhang and Ren, 2025). Therefore, it is necessary to conduct an operability analysis in shallow waters. However, previous research has not engaged in parametric study of operable environmental conditions (ECs) for caisson towing (Jiang et al., 2018; Verma et al., 2020; Wang et al., 0000).

Variations in seabed topography or bathymetry in shallow waters significantly influence the motion response of floating structures across all degrees of freedom (Belibassakis, 2008; Magkouris et al., 2021; Chen et al., 2025; Liu et al., 2023). Therefore, it is crucial to consider the effects of seabed slope and aspect when calculating the response of a marine floating structure in shallow water. Under the assumption of slowly varying bathymetry and based on three-dimensional potential flow theory with linearized free-surface boundary conditions, a mild slope model was developed to analyze wave-induced motion (Takagi et al., 1994). To extend the applicability to larger slopes, an expanded mild slope model is proposed here. By discretizing the domain using a simple Rankine source, the boundary element method can be used to address the effects of arbitrary seabed variations without relying on any mild slope assumptions (Belibassakis et al., 2018; Magkouris et al., 2021; Feng et al., 2021, 2019). The seabed can alternatively be incorporated into a panel model as a secondary structure located on the seabed (ten Oever et al., 2014; Ferreira and Newman, 2009; Buchner, 2006). However, early studies regarding the effects of bathymetry variations on floating body motion have lacked experimental validation and comparisons with other numerical methods. Furthermore, in the mild slope model, expanded mild slope model, and simple Green function method, the functions describing the seabed shape must be sufficiently smooth, which may not accurately represent the complex real-world seabed topography.

In this research, a simplified method of incorporating the seabed into a panel model is supplemented by comparisons with computational fluid dynamics (CFD) results. The specific shallow-water seabed is

simplified into a series of wedge modules and a criterion introduced to determine whether each wedge module is passable, thereby constructing a dataset. Constructed by a neural network, a high-dimensional interpolator is employed to identify the passable areas in the shallowwater region. The main contributions and differences are summarized as follows:

- A CDPR-based MTCT methodology is proposed for efficient shallow-water towing operations.
- The influence of slope and aspect on the wave-induced motions of a floating structure is considered as part of a parametric analysis.
- A probabilistic framework is proposed for assessing safe towing regions in specific shallow-water regions through an operability analysis.

This research is organized as follows. Section 2 introduces the concept of the proposed MTCT mechanism, describing the composition of the system and towing operation procedures. Section 3 outlines the system modeling process, proposes a simplified modeling method for complex shallow-water seabed topography, and introduces a process for addressing grounding issues. In Section 4, a probabilistic framework is proposed to analyze passable regions, including a time-domain analysis, extreme value analysis, CFD, and back propagation (BP) neural network. Section 5 compares the potential flow and CFD results of the caisson motion responses, discusses a caisson's passability under different ECs, and calculates the passable regions in a specific shallow-water region. Section 6 concludes the research.

2. Concept of the MTCT mechanism

2.1. System description

The proposed MTCT mechanism consists of three main components: a caisson, multiple jack-up platforms, and a towing system (see Figs. 2 (a) through (c)). The legs of the platforms are driven into the uneven seabed and platforms are considered fixed points. The multi-towline towing system includes a frame cover, multiple towlines, several sets of truss structures, and corresponding hydraulic winches.

Many regions in shallow waters can become obstacles due to the complex seabed topography and grounding obstructions, resulting in the risk of structural damage to caissons. Therefore, satisfactory maneuverability is required for caisson towage in shallow waters to enable effective obstacle avoidance.

As shown in Fig. 2(d), conventional caisson towing uses one or two main towlines that connect the caisson to the tugboat, giving the caisson a large radius of gyration. The risk of grounding grows higher due to the increased number of tugboats involved. Instead, the proposed MTCT system uses a number of towlines to pull the caisson from different directions, increasing the number of actuators and improving operational accuracy, effectively avoiding the occurrence of grounding accidents caused by tugboats. Moreover, due to its fast movement speed, large load-bearing capacity, and high modularity, the

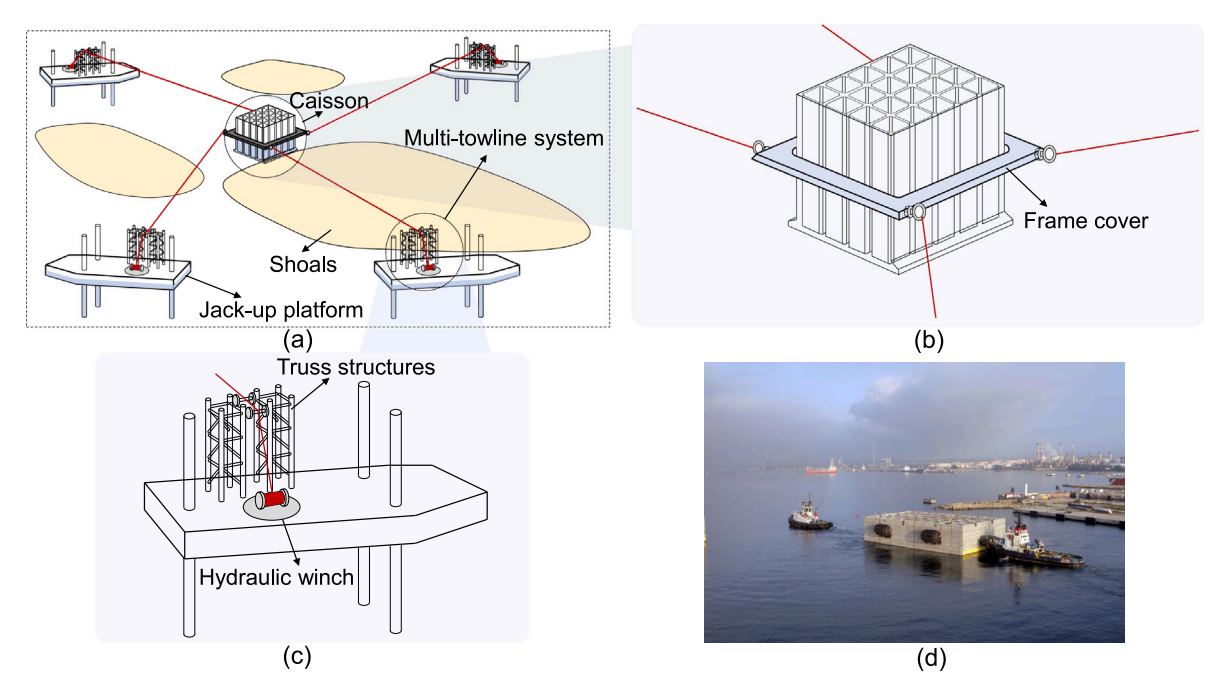


Fig. 2. MTCT concept and conventional caisson-towing operation:(a) MTCT caisson-towing concept, (b) MTCT concept: Towlines connection to the caisson, (c) MTCT concept: zoom in on the multi-towline towing system on the jack-up platform, and (d) conventional caisson towing by tugboats (FCC, 2013).

mechanism is suitable for parallel transportation of large quantities of

The hydraulic winch bases and truss structures are mounted on rotatable turntables. During the caisson towing operation, the tension, direction, and payout/haul-in speed of the towlines can be adjusted based on any errors between the real-time caisson position and predetermined route, further controlling the caisson's speed and heading.

2.2. Towing operations

The entire MTCT towing process can be divided into the following steps:

- Step 1 Preparation of the jack-up platforms: The jack-up platforms are transported to the pre-selected locations. The legs are driven into the seabed to support the platforms above the water surface and the leg-lower distances adjusted to overcome topographic variations in shallow waters.
- Step 2 Caisson transportation to the designated site: The caissons
 are pre-assembled and processed at the construction yard. They
 are then transported to the starting points in the shallow-water
 region, using large semi-submersible vessels or high-powered tugboats when in deeper waters.
- Step 3 Towline connection: The caisson and frame cover are connected by buckles. One end of each towline is attached to the frame cover and the other end is connected to a hydraulic winch.
- Step 4 Collaborative towing: Hydraulic winches on each platform are adopted to retract and release towlines, controlling the caisson's movement along the pre-determined route.
- Step 5 In place: The frame cover is unbuckled to release the caisson after arrival at the designated site.
- Step 6 The frame cover is transported to the next caisson via the retraction towlines and Steps 3 through 5 are repeated.

The jack-up platforms are equipped with sensors (e.g., GPS, tension meters) to monitor position, load, and ECs, and the data fed into the control system. High-capacity hydraulic winches are used to enable precise adjustments to towline tension, payout, and haul-in speeds, dynamically responding to real-time inputs such as wave-induced caisson

movement. Towlines, typically made of high-strength synthetic fibers (e.g., HMPE, Kevlar), are employed to minimize sag and drag in water. Algorithms can then optimize towline tension in real time to reduce energy consumption and risks such as grounding and excessive drift.

The complex seabed topography makes it difficult to construct a refined seabed panel model based on potential flow theory. Substantial variations in topography can easily result in non-convergent calculations. Moreover, the introduction of a high number of seabed panels results in low calculation efficiency. In this study, we focus on the problem of caisson towing in shallow waters (Step 4).

3. Problem formulation

3.1. Seabed topography simplification

A seabed topography simplification approach is adopted here as a means of overcoming the problems associated with constructing a whole seabed panel model. Slope and aspect are key parameters when describing seabed topography. Variations in the seabed topography cause changes in seabed boundary conditions, which in turn influence caisson hydrodynamics. The effects of seabed slope and aspect on a caisson's hydrodynamic response are taken into account in the process proposed here, and seabed topography is simplified into a series of wedge modules.

The seabed topography simplification method is illustrated in Fig. 3. A bathymetry map for a specific shallow-water region can be obtained from public bathymetry data, onsite measurements, etc. Due to data resolution, water depth at only a limited number of points can be known. Hereinafter, these points represented by known bathymetry will be referred to as elevation data points (EDPs). For each EDP, a simplified wedge module is constructed based on its corresponding water depth, slope, and aspect. Then, the bathymetry map is converted into a series of wedge modules. In the potential flow software WAMIT, the wedge module is set as a fixed submerged body. This approach transforms the hydrodynamic coupling effect between the caisson and seabed into that effect between the caisson and a series of simplified wedge modules.

Three right-hand reference frames are then defined (see Fig. 4).

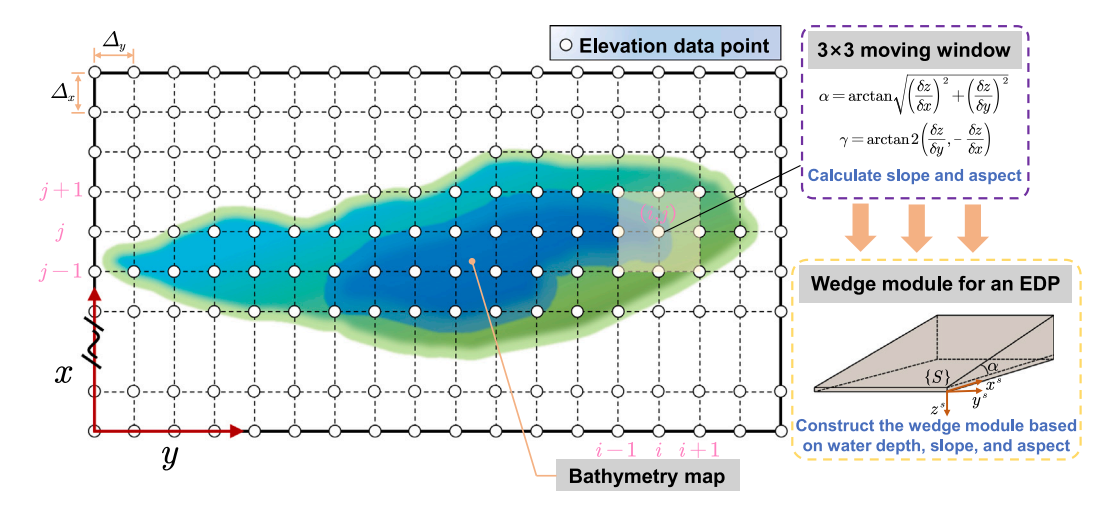


Fig. 3. Seabed topography simplification.

- North-east-down (NED) reference frame $\{N\}$: The origin O is located at the equilibrium point on the free water surface, where the caisson is at rest (i.e., it is not subject to any environmental loads or external disturbances). The x-, y-, and z-axes are northward, eastward, and downward, respectively. The rotations about the x-, y-, and z-axes are named $\operatorname{roll}(\phi)$, $\operatorname{pitch}(\theta)$, and $\operatorname{yaw}(\psi)$, respectively.
- Caisson body-fixed reference frame $\{B\}$: The origin O^b is located at the caisson center of gravity (COG) and the x^b -, y^b -, and z^b -axes are along the length of the caisson, the width of the caisson, and downward, respectively.
- Wedge module-fixed reference frame $\{S\}$: The wedge module is fixed and the origin O^s is located at the bottom vertex of the wedge module. The x^s -, y^s -, and z^s -axes are along the length, width of the wedge module, and downward, respectively.

An overview of the simplified system model is presented in Fig. 4. The aspect γ of a certain wedge module is defined as the rotation angle of $\{S\}$ relative to $\{N\}$ around the z-axis and the wave direction β_w is defined as the angle between the wave propagation direction and the positive direction of x^b .

According to the data processing of the digital elevation model, the Horn's method can be used to calculate the slope and aspect (Cadell, 2002). A 3×3 local moving window is considered, including the center EDP and the surrounding eight EDPs, as presented in Fig. 3. The slope and aspect of the center EDP can be calculated by

$$\alpha_{i,j} = \arctan\sqrt{(\frac{\delta z}{\delta x})^2 + (\frac{\delta z}{\delta y})^2},$$
 (1)

$$\gamma_{i,j} = \arctan(\frac{\delta z}{\delta v}, -\frac{\delta z}{\delta x}),$$
 (2)

where i and j are the indexes of the EDPs in the y- and x-directions, respectively, γ denotes the aspect (i,e., the orientation of the wedge module), $\arctan(\cdot)$ is the inverse tangent function, and $\arctan(\cdot)$ represents the orientation angle from O to the point $(\frac{\delta z}{\delta y}, -\frac{\delta z}{\delta x})$ (i.e., the angle with the x-axis). The change rates along the x- and y-axes, $\frac{\delta z}{\delta x}$ and $\frac{\delta z}{\delta y}$, can be calculated using the third-order inverse distance square weighted difference algorithm,

$$\frac{\delta z}{\delta x} = \frac{(z_{i-1,j+1} - z_{i-1,j-1}) + 2(z_{i,j+1} - z_{i,j-1}) + (z_{i+1,j+1} - z_{i+1,j-1})}{8\Delta_x},$$
 (3)

$$\frac{\delta z}{\delta y} = \frac{(z_{i-1,j-1} - z_{i+1,j-1}) + 2(z_{i-1,j} - z_{i+1,j}) + (z_{i-1,j+1} - z_{i+1,j+1})}{8\Delta_y},$$
 (4)

where Δ_x and Δ_y are the resolutions of the EDPs in x- and y-directions, respectively.

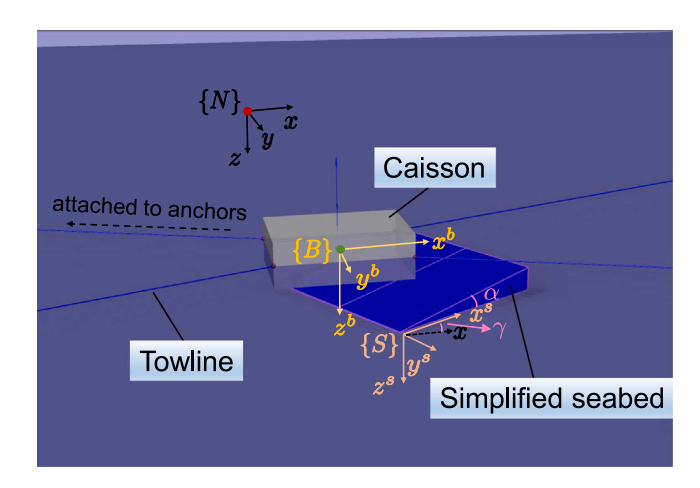


Fig. 4. The simplified system model and reference frames.

3.2. System modeling

To facilitate an understanding of the dynamics of complicated systems, the model is simplified according to several assumptions:

- (1) The structural deflection of the caisson is relatively small compared to its hydrodynamic response. Therefore, the caisson is considered to exhibit rigid behavior and is modeled as a rigid body.
- (2) During the towing process, the frame cover and the caisson are integrated and can be regarded as a rigid connection. Consequently, the frame cover is not included in the modeling and the towlines are connected directly to the caisson.
- (3) The jack-up platforms, truss structures, and hydraulic winches act as frames and are reduced to fixed points.
- (4) The towing speed is assumed to be low, allowing it to be approximated using frequency-domain hydrodynamic results at zero speed. The hydrodynamic results under zero-speed conditions are validated to be more conservative at the general towing speed of the caisson.
- (5) To ensure the accuracy of the hydrodynamic coupling between the caisson and wedge modules in the frequency domain, the towing capacity (namely, retracting and releasing towlines operation) is neglected. The towlines are modeled as linear springs.

3.3. Minimum and characteristic distances

Time-domain simulations are performed and the time series of the caisson COG position determined. The four bottom corners of the caisson are most likely to hit the seabed and be damaged during towing; thus, they are considered when performing the grounding detection between the caisson and wedge modules. The positions of the four bottom corner points, hereinafter referred to as interesting points (purple dots in Fig. 5), can be calculated by

$$p_{e}(t) = p_{b} + R_{b}^{n}(\phi, \theta, \psi) l_{e}^{b}, \tag{5}$$

where $e \in \{1,2,3,4\}$ represents the eth interesting point, p_e is the position of the eth interesting point in $\{N\}$, p_b is the caisson COG position in $\{N\}$, $R_b^n \in \mathbb{R}^{3 \times 3}$ is the rotation matrix from $\{B\}$ to $\{N\}$, and l_e^b is the position of the eth interesting point in $\{B\}$. It is assumed that the coordinates of the four vertices on the topside of the wedge module at $\{S\}$ (red dots in Fig. 5) are p_τ^s , $\tau \in \{1,2,3,4\}$. The positions of the four vertices in $\{N\}$ are

$$p_{\tau} = p_{ns} + R_s^n(0, 0, \psi - \gamma)p_{\tau}^s, \tag{6}$$

where p_{ns} is the position of O^s in $\{N\}$, $p_{\tau} = [x_{\tau}, y_{\tau}, z_{\tau}]^{\mathsf{T}}$, and $R_s^n \in \mathbb{R}^{3 \times 3}$ is the rotation matrix from $\{S\}$ to $\{N\}$, which is represented by

$$R_{s}^{n}(0,0,\psi-\gamma) = \begin{bmatrix} \cos(\psi-\gamma) & -\sin(\psi-\gamma) & 0\\ \sin(\psi-\gamma) & \cos(\psi-\gamma) & 0\\ 0 & 0 & 1 \end{bmatrix}.$$
 (7)

According to p_{τ} , the plane equation describing the topside can be constructed by

$$z = \frac{n_x(x_\tau - x) + n_y(y_\tau - y) + n_z z_\tau}{n_z},$$
(8)

$$n = (p_1 - p_2) \times (p_2 - p_3), \tag{9}$$

where $n = [n_x, n_y, n_z]^T$ is the topside normal vector of the wedge module and the vertical distance of the projection point \mathcal{P}_r on the topside Γ for the eth interesting point can be expressed as

$$z_{proj,\tau}(t) = \frac{n_x(x_\tau - x_e) + n_y(y_\tau - y_e) + n_z z_\tau}{n_z}.$$
 (10)

The vertical distance between the eth interesting point and projection point can be calculated by

$$d_e(t) = \begin{cases} z_e - z_{proj,e}(t), & \mathcal{P}_r \in \Gamma, \\ z_e - D, & \text{otherwise.} \end{cases}$$
 (11)

The minimum distance can be defined by

$$D_{\tau}^{ext} = \min(d_e(t)), t \in [1, T_{sim}], e \in \{1, 2, 3, 4\},$$
(12)

where T_{sim} is the simulation time length and D_z^{ext} is the minimum distance between the interesting points and their projections during the entire time domain simulation. A specific number of random seeds are used to conduct extreme value analyses on the minimum distance. The characteristic distance D_{char} is defined by a given non-exceedance probability.

3.4. Problem statement

It is worth mentioning that the water depth D is defined as the z-axis distance from the mean sea level to the topside of the wedge module, as shown in Fig. 5. In order to avoid difficulties in meshing the sharp part, the front end is cut a small amount δz . The dimensions of the wedge module are determined based on the dimensions of the caisson and water depth.

To ensure that the slope's influence on the caisson is maintained, the length and width of the wedge module should exceed the dimensions of the caisson. Additionally, the top of the wedge module must remain submerged below the water surface.

ECs are defined as the different combinations of wave direction angle β_w , significant wave height H_s , peak period T_p , water depth D, slope α , and aspect γ , which can be expressed as

$$C = \left\{ (\beta_{w}, H_{s}, T_{p}, D, \alpha, \gamma) \mid \beta_{w} \in [\underline{\beta_{w}}, \overline{\beta_{w}}], H_{s} \in [\underline{H_{s}}, \overline{H_{s}}], \right.$$

$$\left. T_{p} \in [\underline{T_{p}}, \overline{T_{p}}], D \in [\underline{D}, \overline{D}], \alpha \in [\underline{\alpha}, \overline{\alpha}], \gamma \in [\underline{\gamma}, \overline{\gamma}] \right\},$$

$$(13)$$

where (\cdot) and (\cdot) denote the lower and upper limits for a specific parameter, respectively.

The objective of this research is to obtain the passable region of a designated caisson under specific sea conditions in a particular shallow-water region, using known bathymetry data. The goal is to rapidly evaluate the passable regions for caisson towing in shallow waters with complex seabed topographies, focusing on the critical impacts of seabed slope, aspect, and wave peak period on towing safety. Concentrating on these key variables enhances the study's precision and efficiency. Moreover, the current framework is adaptable and future studies can incorporate additional environmental factors to improve applicability.

Secondary factors such as ocean currents, wind forces, and fine-scale depth variations could to some extent influence the results. For instance, ocean currents might increase drag and lateral forces, affecting towing path stability; wind forces could induce sway and pitch, reducing maneuverability; and fine-scale depth variations might amplify local hydrodynamic effects, raising grounding risks. These factors are excluded here to simplify the model and validate the analytical framework.

4. Methodology

4.1. Overview

Fig. 6 presents the probabilistic framework for determining passable regions during MTCT caisson towing. For all ECs, frequency-domain response amplitude operators (RAOs) are obtained via the additional damping correction determined by the CFD results. Time-domain simulations are performed to obtain real-time caisson COG positions. After coordinate transformation and an extreme value analysis, the characteristic distances under different ECs are calculated, constructing the dataset with conditions as input and characteristic distances as output. A BP neural network is then applied to determine the nonlinear relationship and serve as an interpolator to obtain the passable regions for specific shallow waters with preset safe boundaries.

4.2. RAO calculation using potential flow theory

Potential flow theory is based on the basic assumptions of inviscid and irrotational fluids. Total velocity potential φ satisfies the Laplace equation

$$\nabla^2 \varphi = 0. \tag{14}$$

The total velocity potential $\varphi(x, y, z, t)$ is subject to physical boundary conditions on a body wet surface S_b , free surface S_f , and seabed S_0 , which can be expressed as

$$\frac{\partial \varphi}{\partial n_b} = V_{n_b} \text{ on } S_b, \tag{15a}$$

$$\frac{\partial \varphi}{\partial z} - \frac{\partial \eta}{\partial t} = 0 \text{ on } S_f, \tag{15b}$$

$$\frac{\partial \varphi}{\partial t} + g\eta = 0 \text{ on } S_f, \tag{15c}$$

$$\frac{\partial \varphi}{\partial z} = 0 \text{ on } S_0, \tag{15d}$$

where n_b is the normal vector of the body surface toward the fluid domain, V_{n_b} is the body surface velocity in the direction n_b , and η and g are free surface elevation and gravitational acceleration, respectively.

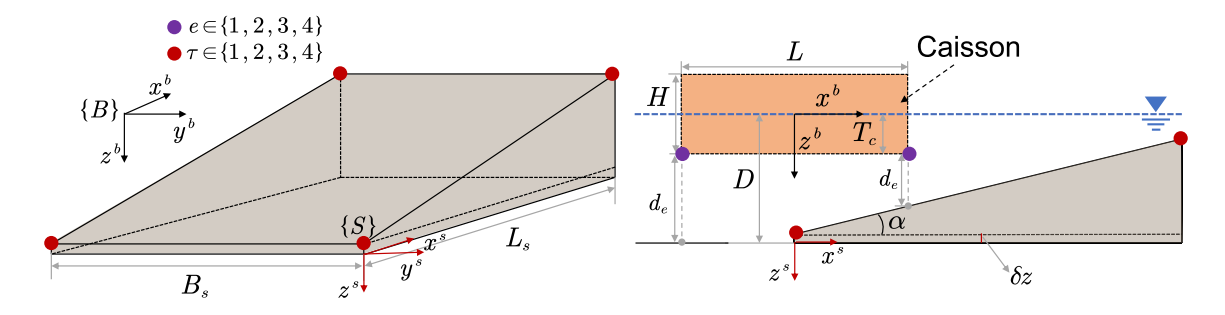


Fig. 5. Dimension of the caisson and the seabed wedge module.

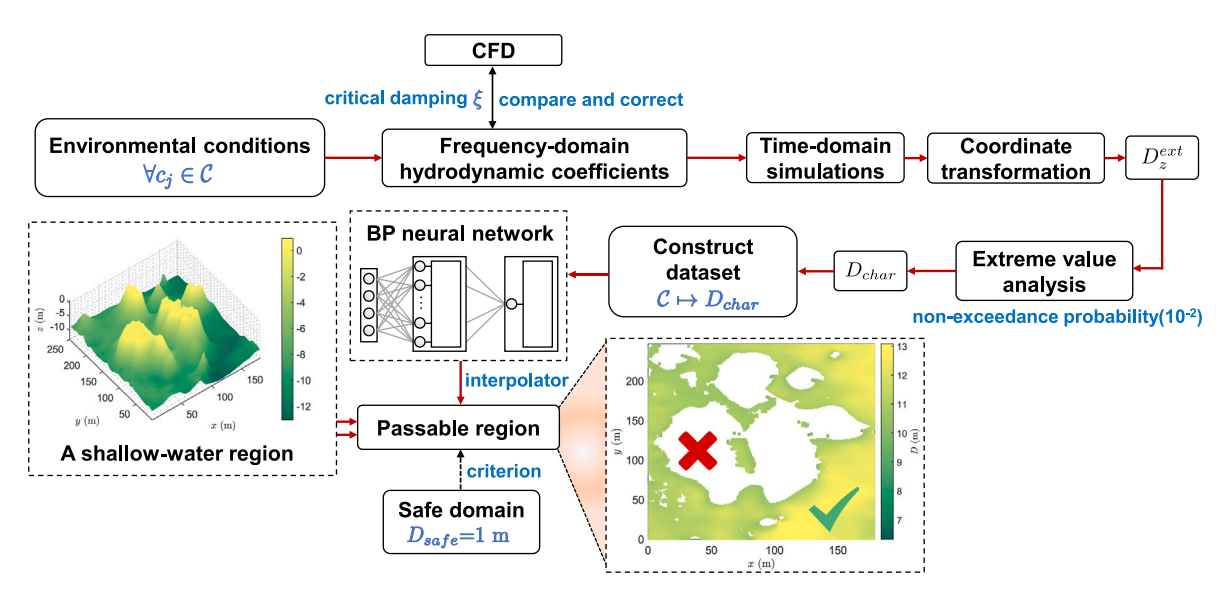


Fig. 6. Overview of the methodology to determine the passable regions.

According to the Bernoulli equation, the hydrodynamic pressure on the body surface p(t) can be calculated by

$$p(t) = -\rho \frac{\partial \varphi}{\partial t},\tag{16}$$

where ρ denotes the fluid density. The frequency-domain Froude–Krylov force F_I and diffraction force F_D can be obtained after p(t) is solved (Liu et al., 2021).

Thus, motion RAOs can be obtained by

$$RAO = \frac{F_I(i\omega) + F_D(i\omega)}{-\omega^2(M + M_a(\omega)) - i\omega B(\omega) + K_s},$$
(17)

where $M \in \mathbb{R}^{6\times 6}$ is the rigid mass matrix of the caisson, ω is the angular frequency of incident waves, $M_a \in \mathbb{R}^{6\times 6}$ is the added mass, $B \in \mathbb{R}^{6\times 6}$ is the radiation damping, and $K_s \in \mathbb{R}^{6\times 6}$ is the hydrostatic restoring matrix.

4.3. RAOs correction using the CFD method

In order to correct the calculation results of the constructed potential flow model, StarCCM+ is used to establish a numerical wave tank and calculate the caisson hydrodynamic responses for the wedge module in shallow waters. An unsteady incompressible Reynolds-averaged Navier–Stokes approach is applied. The volume of fluid method is used to capture the air–water free surface. It is recommended to use 60 to 80 grids per wavelength and 12 to 20 grids per wave height to ensure accurate waveform capture without over-densifying the grid. The caisson is considered a rigid body and the interaction between the caisson and fluid is simulated using the dynamic fluid body interaction

model. The caisson parameters are consistent with the settings in potential flow theory.

Due to the absence of a mooring system, allowing the surge degree of freedom in head-sea conditions would cause the caisson to drift away under wave action, making it impossible to achieve the desired results. Therefore, under head-sea conditions, only the heave and pitch degrees of freedom of the caisson are allowed.

4.3.1. Computational domain

The boundary condition setting is shown in Fig. 7(a). An inclined segment is set to represent the sloped seabed. The inlet and outlet in the computational domain are both set as velocity boundaries, and the sloped bottom is set as a no-slip wall. The two sides are set as symmetry conditions and pressure condition is applied to the top boundary. The size of the calculation domain is taken as $9.3L \times 2.67L$, as per to the recommendation of the International Towing Tank (Recommended ITTC, 2011), where L is the caisson length. The detailed dimensions of the calculation domain are shown in Fig. 7(b).

An overset mesh technique is used to realize the movement of the caisson in the fluid domain, as shown in Fig. 7(c). The overset mesh technique involves using a background mesh for the entire computational domain and an overlapping body-fitted mesh for the solid body to allow for flexible and accurate simulation.

4.3.2. Response amplitude operator

By stimulating the caisson with long-crested waves for a specific period, the caisson responses across a specific degree of freedom can be obtained as well as the wave-response transfer function (i.e., the RAO)

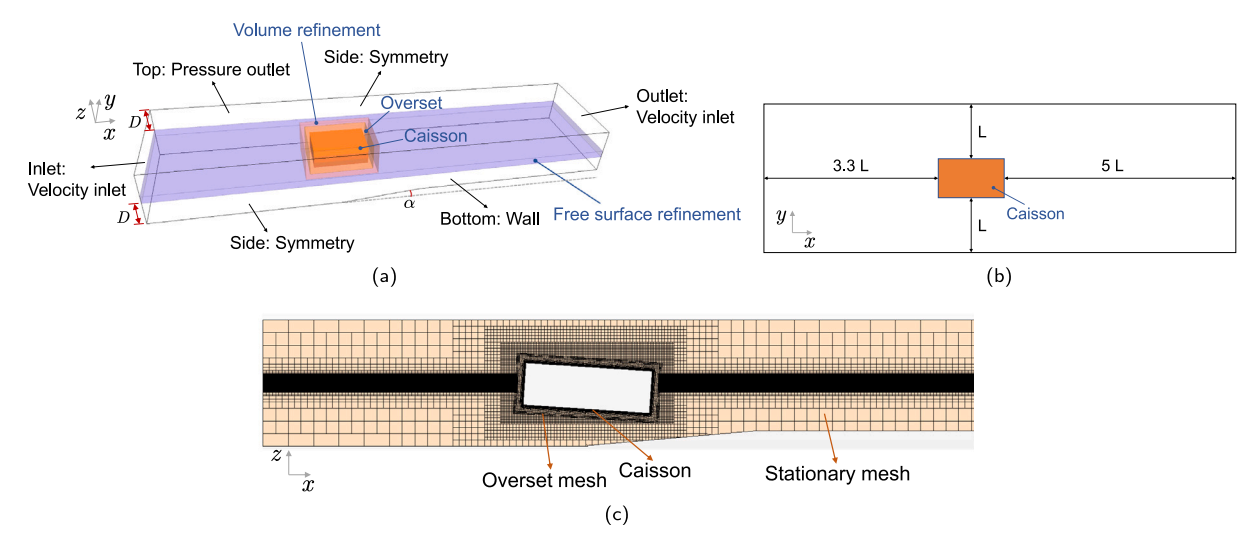


Fig. 7. System configuration in CFD: (a) Boundary conditions, (b) dimension of computation domain, and (c) computational mesh.

under the corresponding wave period can be obtained. For a given wave period, the caisson RAOs in heave and pitch can be calculated by

$$RAO_{heave} = \frac{\eta_1}{H_I},\tag{18}$$

$$RAO_{pitch} = \frac{\eta_2}{H_I},\tag{19}$$

where η_1 and η_2 are the heave and pitch motion amplitudes, respectively, and H_I is the wave height of the incident wave.

4.3.3. Determination of the additional damping

The model is based on potential flow theory, which only considers radiation damping; viscous damping is ignored. Viscosity correction is necessary when using potential flow theory; otherwise, the motion amplitude near the natural period could be very large, deviating from the actual situation (Zhang et al., 2023). The critical damping method is used to perform damping correction on the two degrees of freedom and additional damping is added to the damping terms. The additional damping is determined by

$$B_{a,j_d} = 2 \cdot \xi \cdot \sqrt{(M_{j_dj_d} + M_{a,j_dj_d}) K_{s,j_d}}, j_d = 3, 4, 5,$$
 (20)

where j_d is the j_d th degree of freedom of the caisson, ξ is the critical damping coefficient, $M_{j_dj_d}$ is the (j_d,j_d) item of the rigid body mass matrix, M_{a,j_dj_d} is the (j_d,j_d) item of the added mass matrix under the natural period, and K_{s,j_d} is the hydrostatic restoring force of the j_d -th degree of freedom. The value of ξ can be chosen according to the proximity of the results to potential flow theory and CFD.

4.4. Time-domain simulations

The added mass and radiation damping are calculated in the frequency-domain and the results are then applied to a two-body coupled motion analysis in the time-domain through retardation functions. The second-order wave loads for surge, sway, and yaw are obtained according to Newman's approximation.

A time-domain model based on Cummins equation (Cummins, 1962) with zero forward speed can be established as follows:

$$(M + M_a(\infty))\ddot{x}_c(t) + \int_0^t K(t - \tau)\dot{x}_c(\tau)d\tau + B_a\dot{x}_c(t)$$

$$+ K_s x_c(t) = F_{wave1}(t) + F_{wave2}(t) + F_{towline}(t),$$
(21)

where $M_a(\infty) \in \mathbb{R}^{6\times 6}$ denotes the added mass matrix at the infinite frequency; $x_c(t) \in \mathbb{R}^6$ refers to the vector of time-domain caisson

motion, $K(t) \in \mathbb{R}^{6\times 6}$ is the matrix of retardation functions (i.e., the impulse response functions serving as the kernel of the convolution term that represents the fluid memory effects), B_a is the additional damping in Eq. (20), $F_{wave1}(t) \in \mathbb{R}^6$ and $F_{wave2}(t) \in \mathbb{R}^6$ are the first-and second-order wave-induced loads, respectively, and $F_{towline}(t) \in \mathbb{R}^6$ is the tension in the towlines.

4.5. Extreme value analysis

4.5.1. Regional frequency analysis

The probability distribution of a random variable describes the probability that the variable is equal to a specific value and reflects the probabilistic nature of a stochastic process. The non-exceedance probability can be calculated by:

$$F(\lambda) = P(\Lambda \le \lambda),\tag{22}$$

where $F(\lambda)$ is the value of the cumulative probability distribution function at λ and $P(\Lambda \leq \lambda)$ is the non-exceedance probability for the random variable Λ .

If the cumulative probability distribution function is strictly increasing and continuous, it has an inverse function (namely, the quantile function), which represents the value of the random variable when the non-exceedance probability is equal to P_0 . The quantile function is given by:

$$\lambda(P_0) = F^{-1}(P_0). \tag{23}$$

The frequency analysis is used to accurately estimate the quantile function and the quantiles of the unknown overall distribution by analyzing a limited number of samples and fitting a theoretical probability distribution model to infer the underlying feature of the overall distribution. For a more comprehensive introduction to interval frequency analysis, please refer to Hosking and Wallis (1997).

4.5.2. Maximum likelihood parameter estimation of Gumbel distribution

The Gumbel distribution, a theoretical model describing the statistical distribution of extreme values, is widely applied in hydrological and oceanic extreme response analyses. The distribution features distinct forms for minimum and maximum values. For minimum values, the cumulative distribution function, or non-exceedance probability, is expressed as follows when $\lambda = d_z^{ext}$ and $\Lambda = D_z^{ext}$:

$$F(d_z^{ext}) = P(D_z^{ext} \le d_z^{ext}) = 1 - e^{-e^{\frac{d_z^{ext} - \mu}{\sigma}}}, -\infty < d_z^{ext} < \infty,$$

$$\tag{24}$$

where μ and σ are the position and scale parameters of the Gumbel distribution, respectively;both parameters are estimated. The probability density function of the minimum Gumbel distribution is

$$f(D_z^{ext}|\mu,\sigma) = \frac{1}{\sigma}e^{\frac{D_z^{ext}-\mu}{\sigma}}e^{-e^{\frac{D_z^{ext}-\mu}{\sigma}}}.$$
 (25)

Assuming that the random Gumbel variables $D_{z,k}^{\rm ext}$ for $k=1,2,\ldots,N_k$ are independent and follow the minimum Gumbel distribution, their joint probability density function is

$$\mathcal{L}(\mu, \sigma) = f(D_{z,1}^{ext}, D_{z,2}^{ext}, \dots, D_{z,N_k}^{ext} | \mu, \sigma)$$

$$= (\frac{1}{\sigma})^{N_k} e^{\sum_{k=1}^{N_k} \frac{D_{z,k}^{ext} - \mu}{z,\sigma}} e^{-\sum_{k=1}^{N_k} e^{\frac{D_{z,k}^{ext} - \mu}{z,\sigma}}}.$$
(26)

Maximizing a likelihood function is equivalent to maximizing the natural logarithm of the likelihood function. Then the likelihood function can be expressed as

$$\ln \mathcal{L} = -N \ln \sigma + \sum_{k=1}^{N_k} \frac{D_{z,k}^{ext} - \mu}{\sigma} - \sum_{k=1}^{N_k} e^{\frac{D_{z,k}^{ext} - \mu}{\sigma}}.$$
 (27)

Taking the partial derivative of the likelihood function with respect to each parameter to be estimated, the likelihood equation can be obtained by

$$e_1 = \frac{\partial \ln \mathcal{L}}{\partial \mu} = -\frac{N_k}{\sigma} + \frac{1}{\sigma} \sum_{k=1}^{N_k} e^{\frac{D^{ext} - \mu}{2k}} = 0, \tag{28a}$$

$$e_{2} = \frac{\partial \ln \mathcal{L}}{\partial \sigma} = -\frac{N_{k}}{\sigma} - \sum_{k=1}^{N_{k}} \frac{D_{z,k}^{ext} - \mu}{\sigma^{2}} + \frac{D_{z,k}^{ext} - \mu}{\sigma^{2}} \sum_{k=1}^{N_{k}} e^{\frac{D_{z,k}^{ext} - \mu}{\sigma}} = 0.$$
 (28b)

The solutions μ and σ of the likelihood equation are the maximum likelihood estimates. In order to evaluate the parameter estimation model, goodness of fit (GOF) is introduced to describe the degree of fit for the regression line relative to the observed values. GOF is calculated by

$$R^{2} = 1 - \frac{\sum_{k=1}^{N_{k}} (D_{z,k}^{ext} - \hat{D}_{z,k}^{ext})^{2}}{\sum_{k=1}^{N_{k}} (D_{z,k}^{ext} - \overline{D}_{z}^{ext})},$$
(29)

where $\hat{D}_{z,k}^{ext}$ is the minimum distance value obtained by the fitted probability distribution model and \overline{D}_z^{ext} is the average of N_k minimum distance values $D_{z,k}^{ext}$, $k=1,2,\ldots,N_k$. The closer the GOF R^2 is to 1, the more truly the parameter estimation model reflects the distribution of N_k random variables.

4.6. Characteristic distance prediction using a BP neural network

Given a specific bathymetry map, discrete points can display various combinations of slope, aspect, and water depth, making exhaustive calculations of the characteristic distance impractical. Therefore, constructing a higher-order nonlinear relationship between water depth D, slope α , aspect γ , and characteristic distance D_{char} is necessary. Machine learning algorithms can effectively perform these types of higher-order approximations (Zhou et al., 2023; Wang et al., 2025; Deng et al., 2024).

4.6.1. Neural network architecture

A BP neural network is a multi-layer feedforward network trained using the error backpropagation algorithm. It consists of an input layer, hidden layer, and output layer. The input layer has four neurons: water depth D, slope α , aspect γ , and peak period T_p . The output layer contains one neuron, representing the characteristic distance D_{char} . Fig. 8 illustrates the network structure. A single hidden layer structure with 12 neurons, determined through parameter tuning, is chosen to balance simplicity with sufficient nonlinear fitting capability. The Sigmoid activation function is used in the hidden layer to effectively capture the intricate input–output relationship, as its smooth output

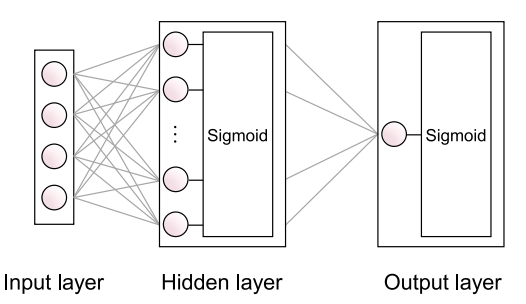


Fig. 8. Architecture of the BP neural network.

range (0,1), combined with data normalization, enhances training stability and ensures the physical interpretability of the predictions. Given the limited training data, Bayesian regularization is used as the training algorithm, offering better control over model complexity and reducing overfitting, as compared to traditional methods like SGD or Adam. This approach ensures robustness in small-sample scenarios while improving the model's generalization to varying input features.

4.6.2. Data preprocessing

In order to speed up the convergence of the network and prevent the output saturation of neurons, the input and output vectors of the network are normalized:

$$x_d^* = \frac{\overline{x} - \underline{x}}{\max(x_d) - \min(x_d)} (x_d - \min(x_d)) + \underline{x},$$
(30)

where \overline{x} and \underline{x} are the upper and lower limits of the normalized interval respectively, x_d are the data that needs to be normalized, and x_d^* are the data after normalization. The input vector is normalized to [0,1] (i.e., \overline{x} and \underline{x} are taken to be 1 and 0, respectively). The output vector is normalized to [-1,1].

4.7. Passable region

For each environmental condition $c_j \in \mathcal{C}$, the corresponding $D_{char}(c_j)$ can be obtained through extreme value analysis. From this, the safe boundary $D_{safe} > 0$ is set. When $D_{char}(c_j) \geq D_{safe}$, the caisson under the corresponding EC c_j is passable; otherwise, it is impassable.

Given a certain sea condition β_w , H_s , and T_p , the passable region can be calculated by

$$C_{safe} = \{c_j \mid D_{char}(c_j) \ge D_{safe}, \forall c_j \in C\}.$$
(31)

5. Simulation results

5.1. Simulation overview

The principal dimensions and parameters of the considered caisson and wedge modules are shown in Table 1. The variables D, α , and γ of the wedge modules are set according to preset conditions and δz is taken to be 0.2 m. The connection points and parameters of the towlines are listed in Table 2. The interesting points $e \in \{1,2,3,4\}$ are the four corner points (i.e., $p_e = (x_e, y_e, z_e) = (15,10,-5), (-15,10,-5), (-15,-10,-5),$ and (15,-10,-5) m, respectively).

Time-domain multi-body simulations are performed via the SIMA workbench. The dynamic analyses are conducted using a 0.01 s sampling interval, with 20 simulations per EC employing distinct random wave seeds. Each 2400 s simulation excludes the initial 600 s during post-processing to eliminate transient effects, yielding an effective duration of 1800 s. The JONSWAP wave spectrum is used, with shortcrested waves applied for time-domain simulations. The target non-exceedance probability is taken as 10^{-2} in the extreme value analysis,

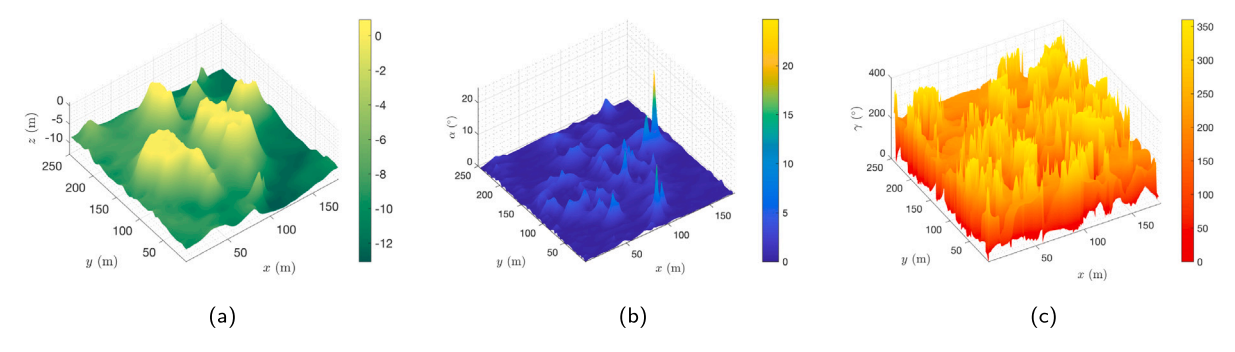


Fig. 9. The considered shallow-water region: (a) Bathymetry, (b) slope, and (c) aspect.

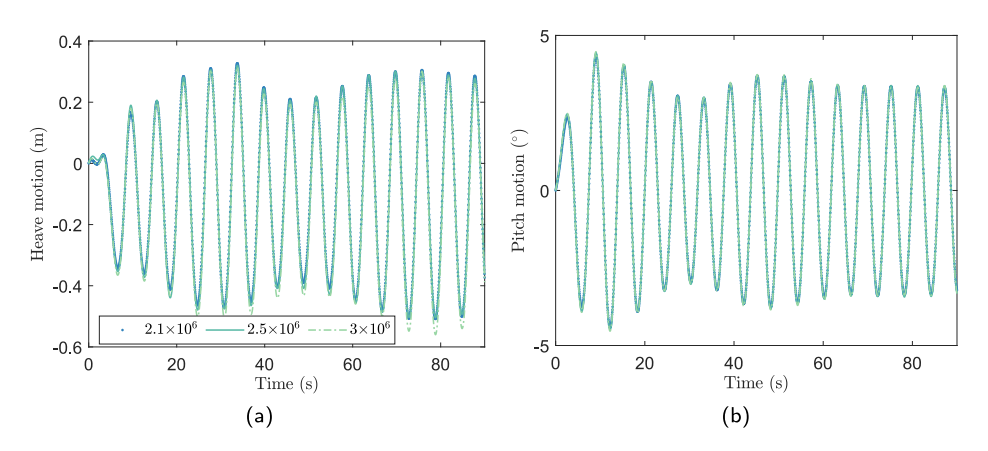


Fig. 10. Mesh convergence at $\alpha = 5^{\circ}$, T = 6 s using different number of meshes in (a) heave and (b) pitch.

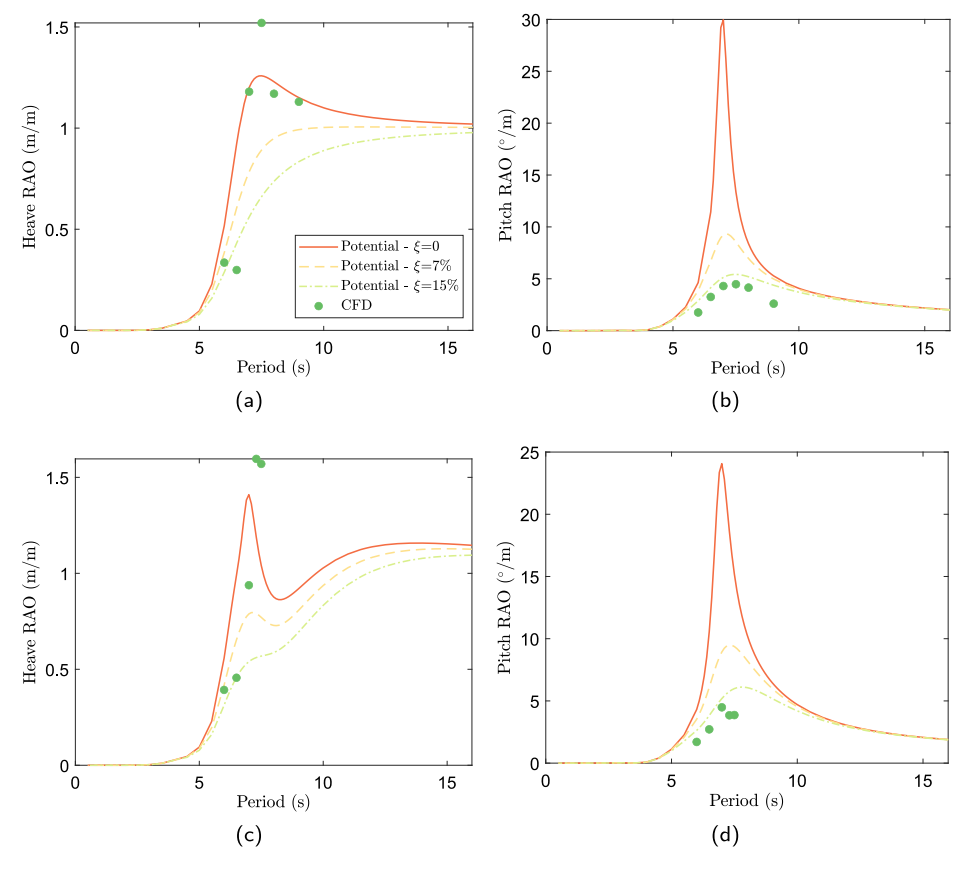


Fig. 11. Potential flow and CFD results of RAOs in (a) heave and (b) pitch at $\alpha=0^{\circ}$, (c) heave and (d) pitch at $\alpha=5^{\circ}$.

Table 1
Selected dimensions and parameters of the caisson and seabed wedge modules.

Object	Parameter	Unit	Symbol	Value
	Length	m	L	30
	Breadth	m	B	20
	Height	m	H	10
	Draft	m	T_c	5
Caisson	Mass	kg	M_c	3.07E6
	Moment of inertia in x^b	kg⋅m ²	I_{xx}	1.28E8
	Moment of inertia in y^b	kg⋅m²	I_{yy}	2.56E8
	Moment of inertia in z^b	$kg \cdot m^2$	I_{zz}	3.33E8
	Length	m	L_s	40
Wedge seabed module	Breadth	m	B_s	40
weage seased module	A small amount at front end	m	δz	0.2

Table 2
Connection points and parameters of towlines.

Parameter	Value
Length of towline (m)	836.85
Linear stiffness (N/m)	2E8
Connection points on caisson in $\{B\}$ (m)	(-15, -10,0), (-15,10,0), (15,10,0), (15, -10,0)
Fixed points in $\{N\}$ (m)	(-800, -300,0), (-800,300,0), (800,300,0), (800, -300,0)

Table 3

Environmental condition groups.				
ECG	D (m)	α (°)	T_p (s)	γ (°)
1	6	0, 2.5	5, 6, 7, 8	0
2	6	0, 2.5	7	45, 90, 135, 180, 225, 270, 315
3	7	0, 2.5, 5, 7.5	5, 6, 7, 8	0
4	7	2.5, 5, 7.5	7	45, 90, 135, 180, 225, 270, 315
5	8	0, 2.5, 5, 7.5, 10	5, 6, 7, 8	0
6	8	2.5, 5, 7.5, 10	7	45, 90, 135, 180, 225, 270, 315
7	9	0, 2.5, 5, 7.5, 10, 12.5	5, 6, 7, 8	0
8	9	5, 7.5, 10, 12.5	7	45, 90, 135, 180, 225, 270, 315
9	10	0, 2.5, 5, 7.5, 10, 12.5, 15	5, 6, 7, 8	0
10	10	2.5, 5, 10, 15	7	45, 90, 135, 180, 225, 270, 315
11	11	0, 2.5, 5, 7.5, 10, 12.5, 15, 16, 17, 18, 19, 20	5, 6, 7, 8	0
12	11	5, 10, 15, 20	7	45, 90, 135, 180, 225, 270, 315
13	12	0, 2.5, 5, 7.5, 10, 12.5, 15, 16, 17, 18, 19, 20	5, 6, 7, 8	0
14	12	5, 10, 15, 20	7	45, 90, 135, 180, 225, 270, 315
15	13	0, 2.5, 5, 7.5, 10, 12.5, 15, 16, 17, 18, 19, 20	5, 6, 7, 8	0
16	13	5, 10, 15, 20	7	45, 90, 135, 180, 225, 270, 315
17	14	0, 2.5, 5, 7.5, 10, 12.5, 15, 16, 17, 18, 19, 20	5, 6, 7, 8	0
18	14	5, 10, 15, 20	7	45, 90, 135, 180, 225, 270, 315
19	15	0, 2.5, 5, 7.5, 10, 12.5, 15, 16, 17, 18, 19, 20	5, 6, 7, 8	0
20	15	5, 10, 15, 20	7	45, 90, 135, 180, 225, 270, 315
21	16	0, 2.5, 5, 7.5, 10, 12.5, 15, 16, 17, 18, 19, 20	5, 6, 7, 8	0
22	16	5, 10, 15, 20	7	45, 90, 135, 180, 225, 270, 315
23	17	0, 2.5, 5, 7.5, 10, 12.5, 15, 16, 17, 18, 19, 20	5, 6, 7, 8	0
24	17	5, 10, 15, 20	7	45, 90, 135, 180, 225, 270, 315

Table 4
Working conditions for the CFD simulations.

D (m)	γ (°)	H_I (m)	α (°)	T (s)
15	0	2	0	6, 6.5, 7, 7.5, 8, 8.5
15	0	2	5	6, 6.5, 7, 7.3, 7.5

 Table 5

 Comparison of simulation results from three different meshes.

Mesh	$N_m/10^4$	Heave (m)	Pitch (°)
M1	210	0.3989	3.3325
M2	250	0.4081	3.5053
М3	300	0.4154	3.5177

meaning that D_z^{ext} will be less than D_{char} once out of every 100 towing operations. The safe boundary D_{safe} is set as 1 m.

Based on a long-term statistical analysis of a specific shallow-water region (see Fig. 9), characteristic wave parameters can be established, including significant wave height $H_s = 1.25$ m and peak periods $T_p = 5$

to 8 s. The region is characterized by water depths $0 \le D \le 13$ m, seabed slopes $0 \le \alpha \le 24.75^\circ$, and aspects $0 \le \gamma \le 360^\circ$. ECs are systematically categorized into environmental condition groups (ECGs), as detailed in Table 3. Each ECG is comprised of multiple ECs; for instance, ECG 1 consists of eight ECs, combining two water depths with four peak periods. The complete analysis encompasses 24 ECGs, totaling 740 ECs.

5.2. CFD simulations

A CFD caisson model with inclined seabed boundary conditions is then established and validated against potential flow results. Working conditions are detailed in Table 4. Mesh convergence analysis is performed using the case of $\alpha=5^\circ$ and T=6 s. As shown in Table 5, the maximum deviation between M1 (coarse mesh) and M2 (medium mesh) is 4.93% in the pitch direction. This deviation reduces to 0.35% between M2 and M3 (fine mesh) for pitch. The largest deviation between M2 and M3 is 1.76%, observed in the heave direction. The variable N_m denotes the total number of meshes.

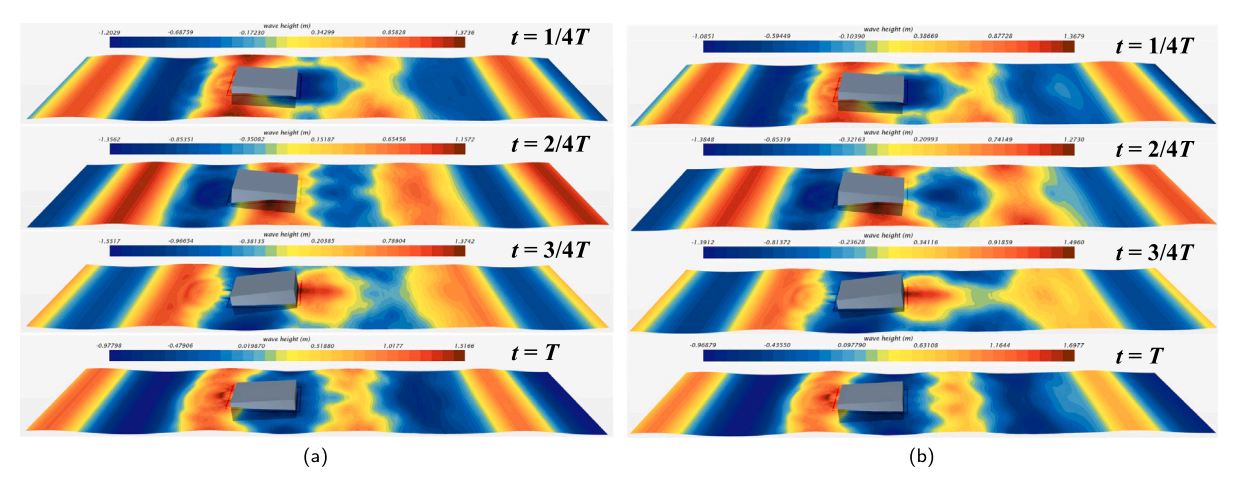


Fig. 12. Visualization of the free surface flow field for T=7 s; (a) $\alpha=0^{\circ}$ and (b) $\alpha=5^{\circ}$.

Fig. 10 demonstrates minimal variation in the results across different mesh densities. Based on the balance between computational accuracy and efficiency, a mesh count of 2.5×10^6 elements is pursued for subsequent analysis.

For the sake of simplification, only waves with head sea ($\beta_w=0^\circ$) are considered, requiring motion amplitude corrections in heave and pitch ($j_d=3,5$ in Eq. (20)). Using the conditions from Table 4, the caisson's RAOs are calculated via Eqs. (18) and (19). Fig. 11 compares potential flow predictions with CFD results across various critical damping coefficients ξ . Optimal agreement between potential flow theory and CFD is achieved with $\xi=0$ for heave RAO and $\xi=15\%$ for pitch RAO and these values are then retained for subsequent potential flow analyses.

The influence of the caisson on the flow field over a flat seabed is shown in Fig. 12(a). It can be observed that the flow field distribution is relatively symmetric along the wave propagation direction, with wave height exhibiting a regular striped pattern. In contrast, the influence of the caisson on the flow field over a sloped seabed is depicted in Fig. 12(b). Due to the presence of the slope, wave refraction and scattering occur during propagation, resulting in an asymmetric flow field and more complex variations in wave height. In the sloped region, waves become focused, leading to a significant increase in local wave height, which is particularly pronounced around the structure. The change in topography breaks the symmetry of the floating structure's influence on the flow field, causing notable differences in wave height distribution between the front and rear.

Overall, the caisson significantly impacts the flow field under both conditions, altering the wave propagation direction and creating notable flow disturbances. However, the sloped seabed intensifies the effect, leading to more pronounced local wave height increases and an asymmetric distribution.

5.3. Frequency-domain RAOs and time-domain simulations

Frequency-domain and time-domain simulations are conducted for all ECs; however, only partial results are shown herein, due to manuscript length limitations. The caisson motion RAOs for heave and pitch are presented in Figs. 13(a) and 13(b) for $\gamma=0^\circ$, D=11 m, and $\beta_w=0^\circ$, with varying slopes. Slope has a significant impact on the motion RAOs in terms of both heave and pitch. As the slope increases, the heave motion amplitude gradually rises. When $\alpha=15^\circ$, the heave RAO peak at the natural period exceeds 2.5 m/m. The trend of the pitch RAO increase with slope is the same as what is seen with heave. Meanwhile, it can be observed that the pitch natural period grows continuously as the slope increases. Moreover, the existence of slope causes a new peak below the natural period for the pitch.

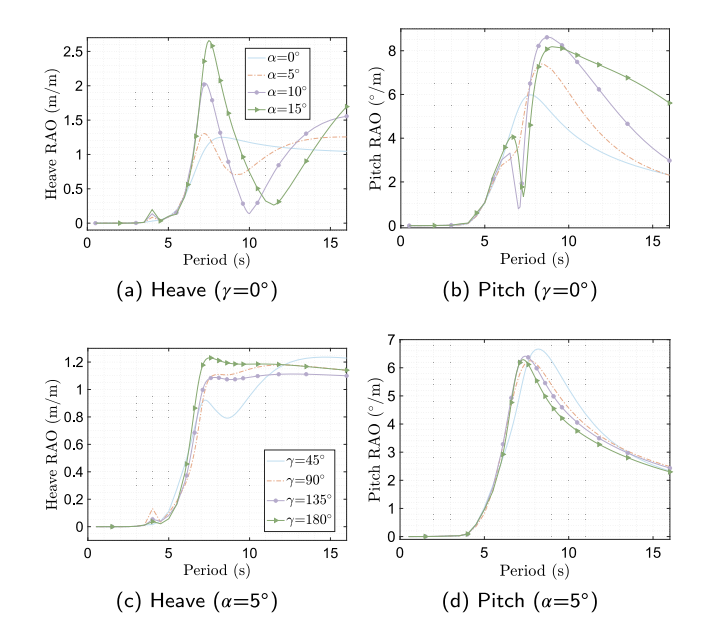


Fig. 13. Motion RAOs for ECGs 11 and 12, with D=11 m and $\beta_w=0^\circ.$

Figs. 13(c) and (d) present the heave and pitch RAOs for $\alpha = 5^{\circ}$, D = 11 m, and $\beta_w = 0^{\circ}$, with varying aspects. Compared to the influence of slope α , aspect γ has a relatively smaller impact on the response amplitudes. Aspect affects both the heave and pitch natural periods. The natural period for pitch gradually decreases as the aspect increases.

Figs. 14(a) and (b) present the heave and pitch motions with respect to α when D=10 m, $\gamma=0^{\circ}$, and $T_p=5$ s and a certain wave random seed is selected. The wave-induced motions in terms of heave and pitch generally increases with an increasing α in most time.

Figs. 15(a) and 15(b) illustrate the motion trajectories of the specified interesting point in the xz-plane. In head seas, the surge motions dominate over the heave and pitch motions, with their influence intensifying at higher peak periods T_p , likely due to second-order drift forces. Heave and pitch motions critically influence grounding assessment by determining the vertical distances between interesting points and their projections. Seabed slope α affects the distances through two mechanisms: steeper slopes increase both heave and pitch motion amplitudes while simultaneously reducing the distances between bottom interesting points and the topside of the wedge module.

In sum, a higher α not only increases the hydrodynamic response of the caisson, it also changes the collision boundary conditions due to changes in water depth.

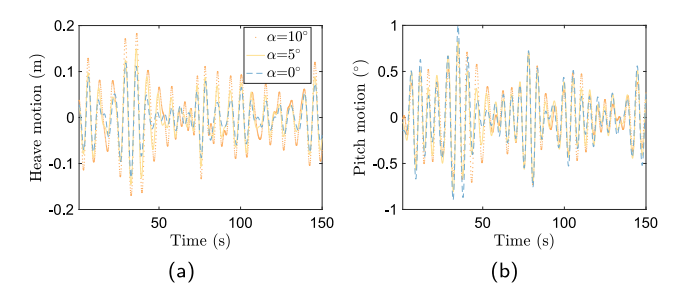


Fig. 14. Response in ECG 9, with D=10 m, $\gamma=0^{\circ}$, and seed=1: (a) Heave and (b) pitch motions at $T_n=5$ s for different α .

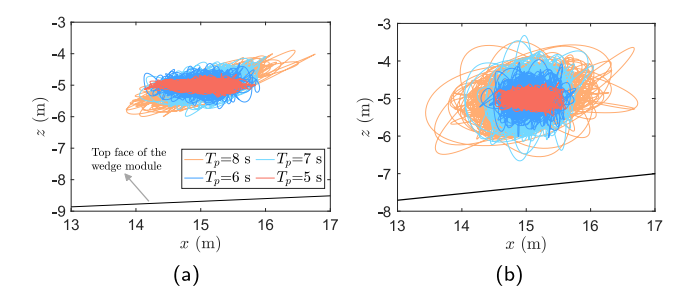


Fig. 15. Motion traces of the caisson interesting point (15,10,-5) in $\{N\}$ for ECG 9, with D=10 m, $\gamma=0^{\circ}$, and seed=1: (a) $\alpha=5^{\circ}$ and (b) $\alpha=10^{\circ}$ for different T_p values.

5.4. Extreme value analysis of minimum distance

Figs. 16(a) and 16(b) present the distance time series between the four interesting points and the corresponding projection points on the wedge seabed module, using a certain random wave seed in ECG 5 with $\alpha=2.5^{\circ}$ and 7.5°. It can be seen that the time series of the interesting points that are symmetrical at about the *x*-axis are almost completely overlapped. This is due to the fact that $\beta_w=0^{\circ}$ and the roll motions are small. The minimum vertical distance is less than zero for EC 5 with $\alpha=7.5^{\circ}$, meaning that groundings with the wedge module do occur.

Extreme value distributions of D_z^{ext} are described in Figs. 16(c) and (d) by the estimated parameters μ and σ in ECG 5 for $\alpha=2.5^\circ$ and 7.5°. Simulations are repeated 20 times using random seeds in each EC. The minimum value of the vertical distance between the caisson's interesting points and the projections is extracted and then fitted by the Gumbel distribution. The extreme value distribution in ECG 5 for $T_p=5$ s is on the rightmost side and that for $T_p=8$ s is on the leftmost side, meaning that the average D_z^{ext} for $T_p=5$ s is larger than that for $T_p=8$ s during the repeated simulations. The GOF of the Gumbel distribution for the minimum distance D_z^{ext} is larger than 0.89.

Figs. 16(e) and (f) show the characteristic distances with regards to slopes α and peak periods T_p for ECG 5. These values are obtained through the minimum Gumbel distribution and the predetermined non-exceedance probability. The black dash-dotted line represents the non-exceedance probability of 10^{-2} and the point where it intersects the fitting curve is the characteristic distance for the specific EC. The safe boundary D_{safe} is set at 1 m, which can be adjusted by taking into account factors such as changes in local tide levels. The characteristic distances for which the values are larger than D_{safe} are marked as green dots, and those values less than D_{safe} are marked as red dots. The characteristic distance is the smallest at $T_p=8$ s and reaches approximately 0.6 m and -2 m at $\alpha=2.5^{\circ}$ and 7.5°, respectively. Furthermore, the characteristic distance increases with the decrease of T_p and the largest value appears at $T_p=5$ s, resulting in a relatively low probability of groundings.

5.5. Characteristic distance under different ECs

Figs. 17(a) through (d) compare the characteristic distances under different peak periods T_p and slopes α for ECGs 5, 9, 13, and 19. It can be observed that for a small slope ($\alpha \leq 2.5^{\circ}$ for D=8 and 10 m and $\alpha \leq 7.5^{\circ}$ for D=12 and 15 m), the characteristic distance D_{char} decreases as T_p increases, indicating that long-period waves pose a threat to the towing safety. For a larger slope, $T_p=7$ s is important (i.e., D_{char} decreases as T_p increases when $T_p \leq 7$ s, but D_{char} increases as T_p increases). The natural periods of the caisson's heave and pitch motions, within the considered range of slopes and aspects are approximately 7 s (see Fig. 13). As a result, the D_{char} adopts 7 s as the critical period, showing opposite variation trends on either side of this value. Additionally, D_{char} generally decreases with an increase of α for all D values. D_{char} is determined by the responses of the caisson and seabed slopes. Its value is dominated by the slopes when T_p is small. In other cases, it is dominated by the responses.

The characteristic distances of the different aspects γ and slopes α for ECGs 6, 10, 14, and 20 are shown in Figs. 18(a) through (d). The characteristic distance D_{char} exhibits approximate symmetry of about $\gamma = 180^{\circ}$ for each slope value, corresponding to the direction parallel to wave propagation (β_w). It is clear that the impact of aspect on characteristic distances D_{char} depends on α . D_{char} slightly changes with an increase in γ when the slope is small ($\alpha = 5^{\circ}$) and the influence of α on D_{char} becomes significant when α is larger ($\alpha = 15$ and 20°). As α increases, the decrease in the free space of the caisson caused by the change in γ is more significant. Specifically, the caisson is more passable under conditions of larger slopes when the aspect $\gamma = 90^{\circ}$ (or 270°), which is due to the caisson's width direction aligning with the wedge module length, and when the caisson length is larger than the width, resulting in a smaller depth variation than the caisson length direction. When α is small (i.e., $\alpha = 5^{\circ}$), the caisson is more passable for $\gamma = 45^{\circ}$ (or 315°).

To access the passability of the caisson under a specific EC using a single parameter (D_{safe}), the characteristic distance is compared to the safe boundary (see Figs. 17 and 18). When D=8 m and $\gamma=0^\circ$, there are five ECs in which the caisson can pass safely. The caisson can pass the wedge module with $\alpha=0^\circ$ and 5° at $T_p=5$ and 6 s, while it can barely pass flat seabed at $T_p=7$ s. For D=12 m, the increased water depth provides a larger passable region for the caisson and it can pass the wedge module successfully with $\alpha \leq 12.5^\circ$. For D=15 m, it can safely pass under all considered α and T_p values. As the aspect varies, the caisson cannot pass under all ECs in ECG 6, and it cannot only pass the wedge module only with $\alpha=20^\circ$, $\gamma=135^\circ$, and 225° in ECG 20. These results can support caisson towing in shallow waters by fully using the water depth caused by tide.

5.6. Construction of a higher-order interpolator

The ECs in Table 3 are simulated and analyzed to obtain the corresponding D_{char} , which serves as the dataset for the neural network. In the dataset, there are 740 samples. Of the total, 705 samples are randomly selected as a training set, and the remaining 35 samples are used as the test set to evaluate the approximation accuracy of the trained network. The performance on the test set is presented in Figs. 19(a) and (b). The regression coefficient is 0.998, and the optimal mean squared error (MSE) reaches 9.58×10^{-4} after 429 iterations. Fig. 20(a) presents the regression plot of D_{char} in the test set, with most data points falling within the confidence interval. Figs. 20(b) and (c) show the relative error and its distribution, revealing that the relative error of D_{char} predominantly lies within the range of -10% to 10%.

Furthermore, 30 additional samples are applied as the validation set to validate the generalization ability of the trained network. Note that sample parameters in the validation set (see Table 6) are not included in Table 3. The prediction accuracy of the trained network on the validation set is shown in Figs. 21(a) through (c). It can be seen that

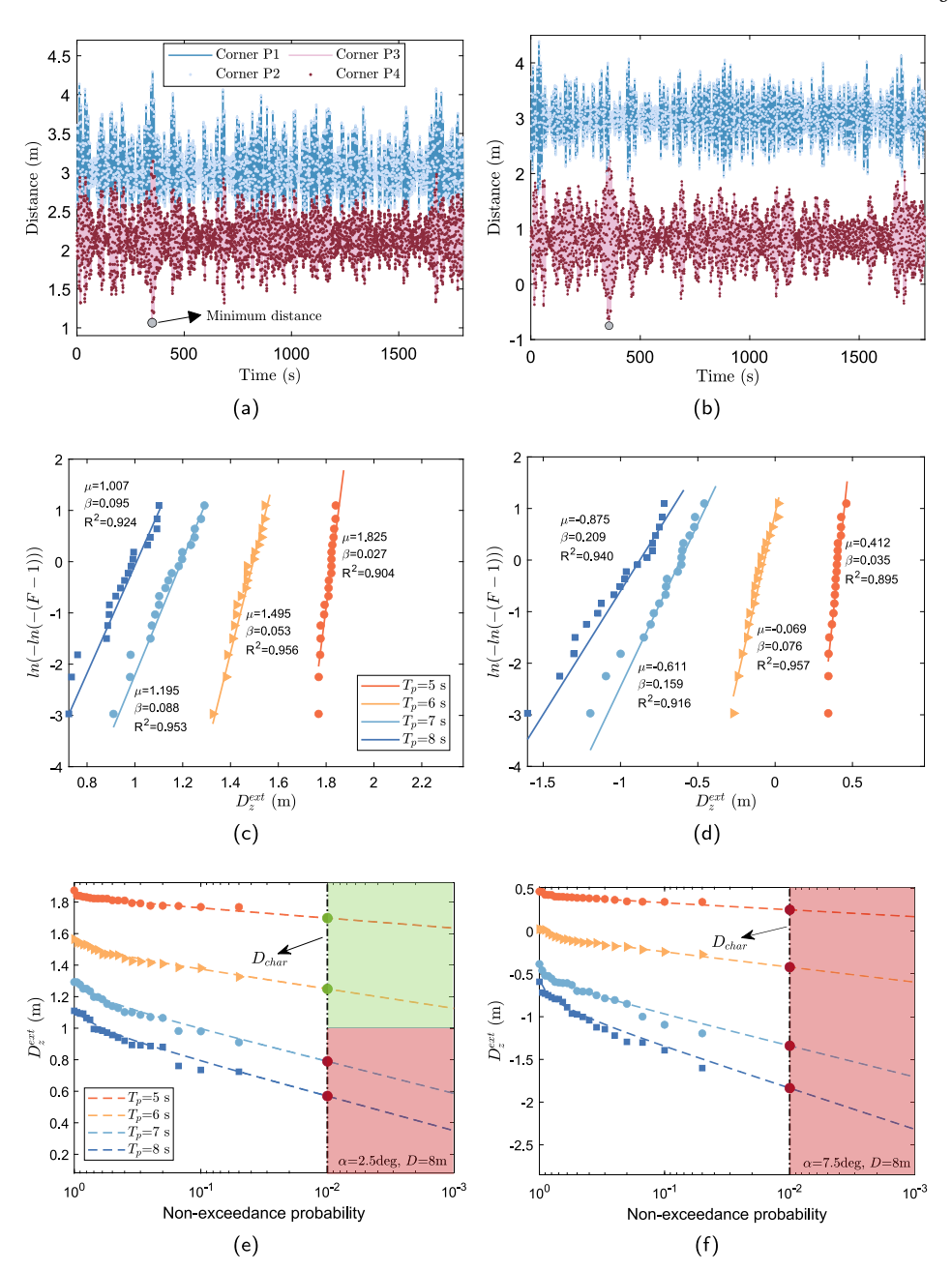


Fig. 16. Vertical distance between four interesting points and their projections on wedge seabed modules (ECG 5, D=8 m) (a) $\alpha=2.5^{\circ}$, $T_p=7$ s, seed=1 and (b) $\alpha=7.5^{\circ}$, $T_p=7$ s, seed=1; Gumbel fitting of minimum distance for (c) $\alpha=2.5^{\circ}$ and (d) $\alpha=7.5^{\circ}$; Characteristic distances for (e) $\alpha=2.5^{\circ}$ and (f) $\alpha=7.5^{\circ}$.

the network performs well with varying α and D values, with regression coefficients close to 1 and MSE values of 4×10^{-4} , and 1.8×10^{-3} , which are close to or better than the optimal MSE (9.58×10^{-4}) in the test set. Fig. 22(a) presents the regression of D_{char} , with most data points falling within the 95% confidence interval. This indicates a strong alignment between the network's predictions and the computed results, demonstrating minimal bias. Figs. 22(b) and (c) illustrate the relative error and its distribution. It can be observed that the relative error of the D_{char} mostly falls within the range of -4% to 6%. However, for the 22nd sample, the relative error reaches as high as 1380%. This is likely due to the calculated value being close to zero, coupled with the limited representation of this type of sample in the training dataset, leading to significant prediction deviations. However, if the safe boundary D_{safe} is set to 1 m, this result does not affect the determination of the passable area.

When dividing the passable region based on D_{safe} , deviations in network prediction accuracy may lead to division errors. For example,

 D_{char} for Sample 23 is close to D_{safe} (pink dotted line), but the network-predicted D_{char} is slightly higher than the calculated value, resulting in a misjudgment. To reduce the occurrence rate, D_{safe} can be appropriately increased to add tolerance, thereby reducing division errors caused by network prediction accuracy deviations. The network performs slightly worse in the γ dimension, due to the limited samples of varied γ . To obtain better prediction accuracy, the original dataset can be further expanded.

In sum, the trained network has satisfying generalization capabilities and meets the requirements of the characteristic distance interpolator.

5.7. Determination of the passable region

In the shallow-water region (shown in Fig. 9), the corresponding characteristic distance for each EDP is obtained based on D, α and γ

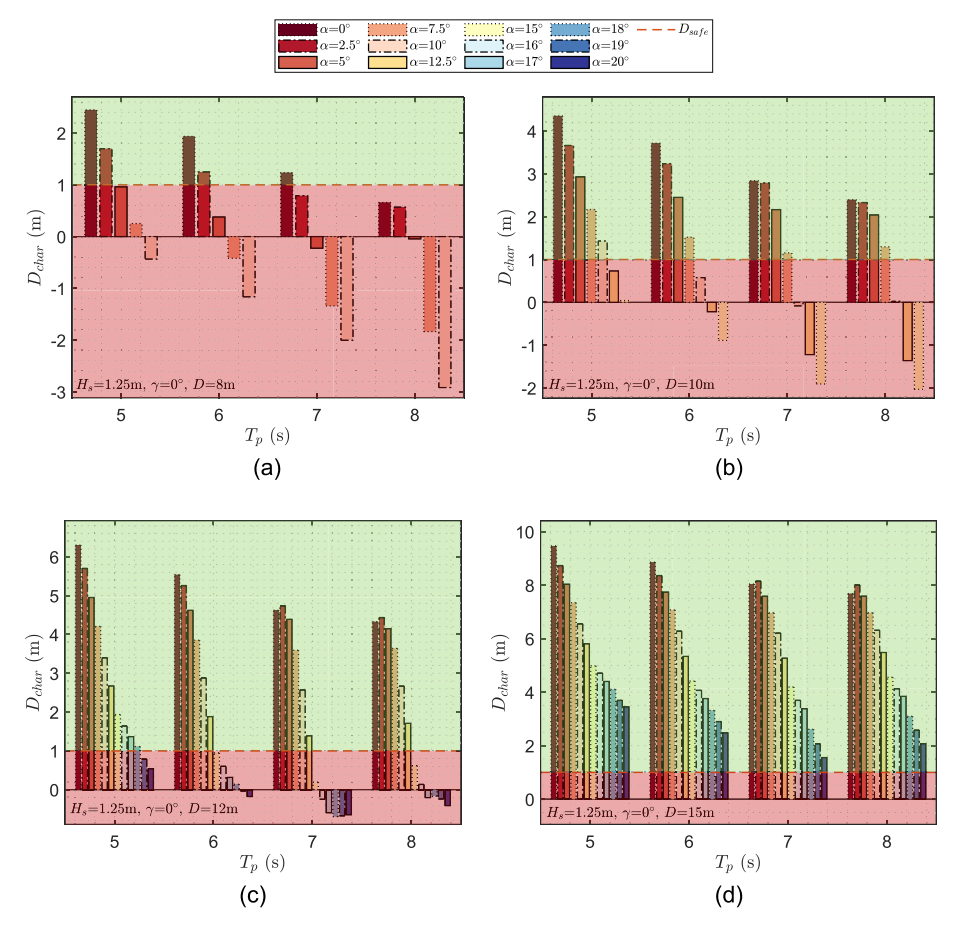


Fig. 17. Characteristic distance w.r.t. α and T_{ρ} in (a) ECG 5, (b) ECG 9, (c) ECG 13, and (d) ECG 19.

Table 6Samples in the validation set.

Sample	D (m)	α (°)	γ (°)
1	17.5	15.5	40
2	17.5	15.5	50
3	17.5	15.5	70
4	17.5	15.5	100
5	17.5	15.5	120
6	17.5	15.5	140
7	17.5	15.5	220
8	17.5	15.5	230
9	17.5	15.5	240
10	17.5	15.5	260
11	15.5	3	30
12	15.5	3.5	30
13	15.5	6	30
14	15.5	6.5	30
15	15.5	8	30
16	15.5	8.5	30
17	15.5	11	30
18	15.5	11.5	30
19	15.5	12	30
20	15.5	12.5	30
21	6.5	3	70
22	7.5	3	70
23	8.5	3	70
24	9.5	3	70
25	10.5	3	70
26	11.5	3	70
27	12.5	3	70
28	13.5	3	70
29	14.5	3	70
30	15.5	3	70

using the constructed interpolator. The results are shown in Figs. 23(a), (d), and (g). Figs. 23(c), (f), and (i) describe the calculated passable region according to the predetermined safe boundary in a specific sea state of $H_s=1.25$ m, $T_p=6.5$, 6.8, and 7 s, and $\beta_w=0^\circ$. The green region represents the passable region, with the depth of color indicating D, while the white region represents the impassable region. To investigate the necessity of considering the slope and aspect for the division of the passable region, the shallow-water region is divided based solely on the minimum D, as presented in Fig. 23(b).

Comparing Fig. 23(b), (e), and (h) to 23(c), (f), and (i), it is evident that D plays a dominant role in determining the passable region. However, the influence of α and γ cannot be ignored.

6. Conclusions

This research proposes a concept of MTCT for caissons and a probabilistic framework of determining the passable regions in specific shallow-water regions. The complicated seabed is simplified into a series of wedge modules and an MTCT time-domain multi-body model for caissons is established. The hydrodynamic coupling effect between the caisson and the wedge module is considered and the frequency-domain results are corrected using a CFD technique. For the shallow-water region under consideration, time-domain simulations are performed under various ECs and the passable region is divided based on a data-driven method. By analyzing the relative vertical distances between the caisson and wedge module during the towing process, the following conclusions are reached:

 The slope and aspect of the seabed significantly influence the hydrodynamic responses of the caisson in the heave and pitch

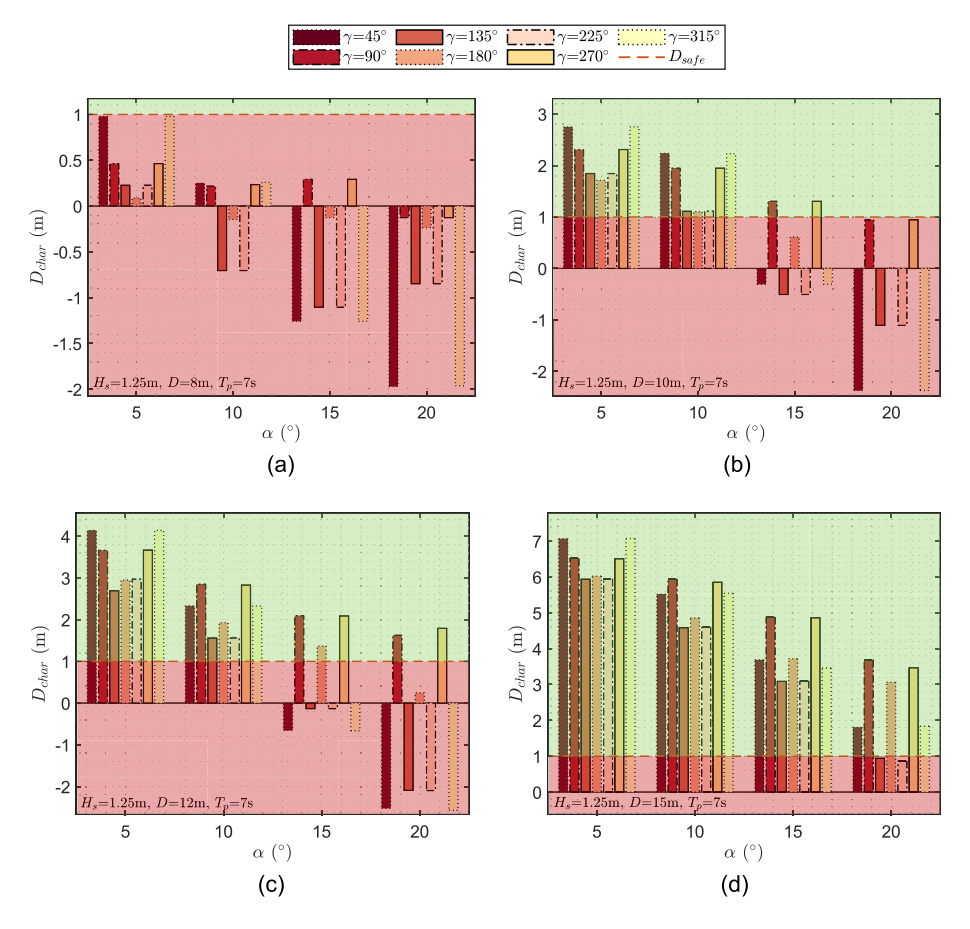


Fig. 18. Characteristic distance w.r.t. α and γ in (a) ECG 6, (b) ECG 10, (c) ECG 14, and (d) ECG 20.

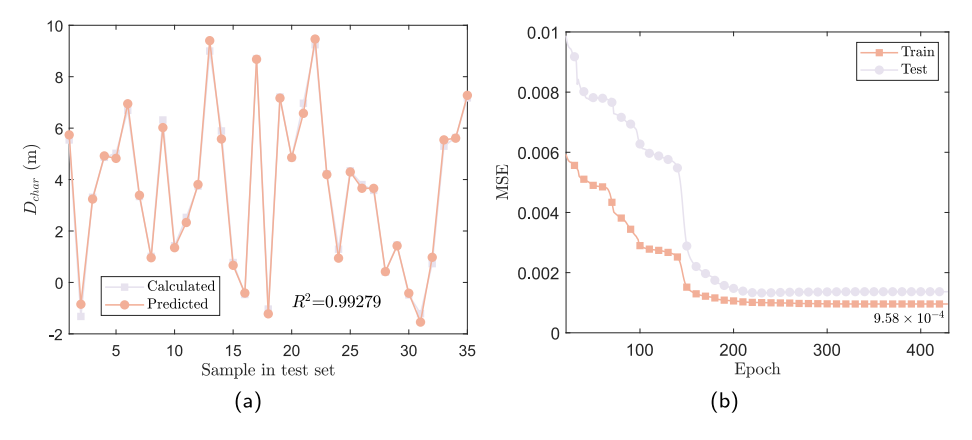


Fig. 19. Prediction performance in (a) regression coefficient and (b) mean squared error.

directions. Changes in slope and aspect not only alter the RAO amplitudes but also affect the natural periods of the heave and pitch motions.

- Simultaneously, variations in slope and aspect also change the collision boundary conditions, resulting in a significant impact when calculating the vertical distance between the interesting points on the caisson and their corresponding projections on the inclined seabed.
- For a non-exceedance probability of 10^{-2} , the vertical distance between the caisson and a 40 m-long seabed (with slopes ranging from 0° to 20°) exceeds the safe boundary at a 15 m water depth and 0° aspect. For water depths of 6 to 17 m and peak period of 7 s, caisson passability for the seabed at aspects of 45° , 135° , 225° , and 315° presents greater challenges under steeper slopes ($\alpha \geq$
- 10°). Within the studied range, a peak period of 7 s represents a critical period for slopes exceeding 2.5° at depths of 8 and 10 m, and for slopes exceeding 7.5° at depths of 12 and 15 m. Caisson passability exhibits approximately linear relationships with water depth and slope (improving with increased depth and decreased slope), while displaying complex, wave-direction-symmetric dependencies on aspect. Wave period influences passability through its modulation of the caisson's hydrodynamic responses (RAO amplitudes).
- The constructed BP neural network effectively maps nonlinear relationships for characteristic distance prediction. The network achieves a regression coefficient of 0.998 and MSE of 9.58×10^{-4} for the test set. Validation results demonstrate strong generalization capability, with regression coefficients approaching 1 for

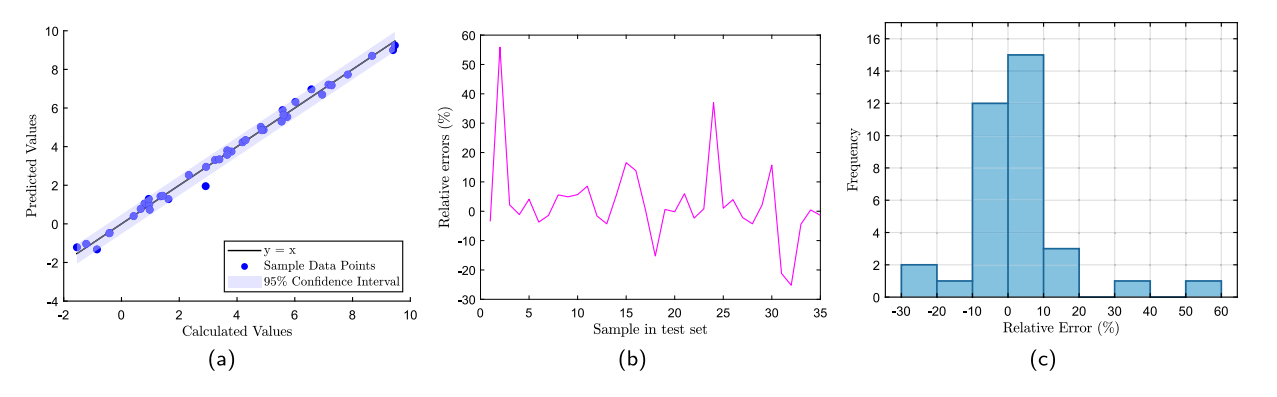


Fig. 20. The comparison between the predicted results and calculated results of D_{char} in the test set. (a) The regression plot, (b) the relative errors, and (c) the distribution of the relative errors.

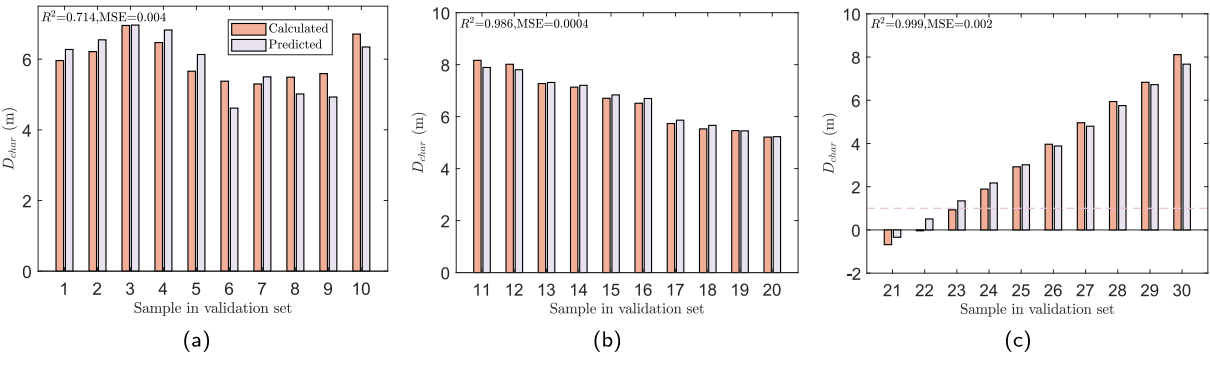


Fig. 21. Prediction performance on the validation set for (a) samples 1-10, (b) 11-20, and (c) 21-30.

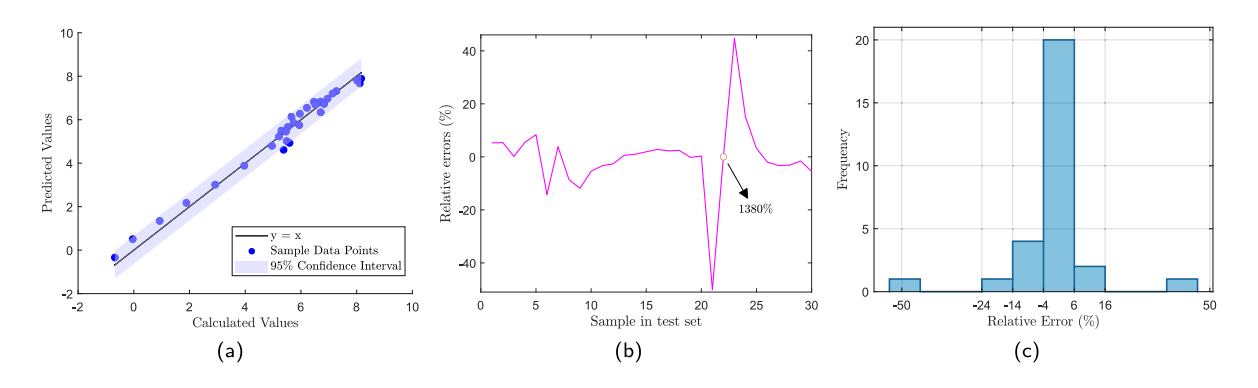


Fig. 22. The comparison between the predicted results and calculated results of D_{char} in validation set. (a) The regression plot, (b) the relative errors, and (c) the distribution of the relative errors.

slope and water depth dimensions, and MSE values comparable to or below the test set optimum. While aspect dimension prediction shows marginally lower accuracy due to limited sampling, its performance metrics remain acceptable.

 Although water depth primarily determines passable regions, both slope and aspect significantly influence operability boundaries.

In this study, caisson hydrodynamic responses near sloped seabeds are calculated using a simplified multi-body coupled potential flow model. The hydrodynamic results are partially validated against CFD simulations within computational constraints. The proposed method for determining passable regions relies on the resolution of seabed

topography data and the accuracy of the calculations based on potential flow theory. $\,$

Future work will focus on enhancing hydrodynamic calculation accuracy for floating bodies near sloped seabeds through advanced potential flow modeling and experimental validation. Incorporating factors such as ocean currents, wind forces, and high-resolution bathymetric data in future studies will enhance the model's applicability in complex real-world sea conditions, providing more precise guidance for caisson towing path planning and risk assessment. Additionally, the fusion of seabed topography data and real-time sea state measurements will provide more precise boundaries for passable regions. The hydrodynamic experimental validation of caissons under sloped conditions was completed in the laboratory and is being prepared for publication.

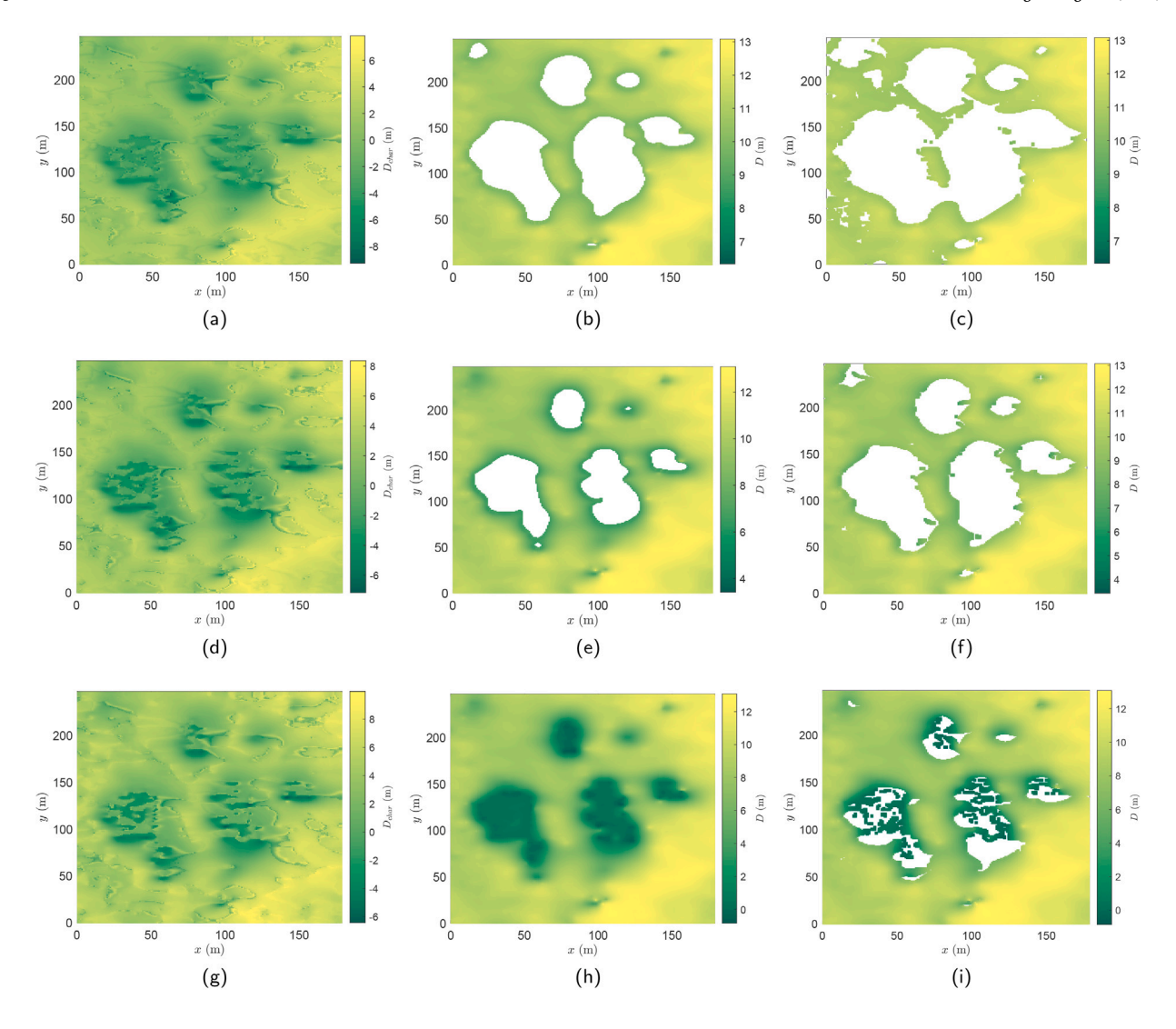


Fig. 23. Passable regions for the selected shallow-water region: Interpolated D_{char} for (a) $T_p = 6.8$ s, and (g) $T_p = 6.8$ s, the regions divided only by D for (b) $T_p = 7$ s, (e) $T_p = 6.8$ s, and (h) $T_p = 6.5$ s, and the divided passable regions for (c) $T_p = 7$ s, (f) $T_p = 6.8$ s, and (i) $T_p = 6.5$ s.

CRediT authorship contribution statement

Zongyuan Yang: Writing – original draft, Visualization, Software, Methodology, Investigation. **Zhengru Ren:** Writing – review & editing, Supervision, Methodology, Funding acquisition, Conceptualization.

Declaration of competing interest

The authors declare that they have no known competing financial interests or personal relationships that could have appeared to influence the work reported in this paper.

Acknowledgments

This research is supported by the National Key Research and Development Program, Ministry of Science and Technology of the People's Republic of China (Grant No. 2022XXX3102603) and Shenzhen Science and Technology Program (Grant No. JCYJ20240813112006009).

References

Alam, M., Guo, Y., Bai, Y., Luo, S., 2025. Post-critical nonlinear vibration of nonlocal strain gradient beam involving surface energy effects. J. Sound Vib. 118930.

Belibassakis, K., 2008. A boundary element method for the hydrodynamic analysis of floating bodies in variable bathymetry regions. Eng. Anal. Bound. Elem. 32 (10), 796–810.

Belibassakis, K., Bonovas, M., Rusu, E., 2018. A novel method for estimating wave energy converter performance in variable bathymetry regions and applications. Energies 11 (8), 2092.

Boskails, 2018. Semisubmersible heavy transport vessels. https://boskalis.com/media/er5hhygw/semi-submersible_heavy_transport_vessels.pdf. (Accessed 15 May 2024). Buchner, B., 2006. The motions of a ship on a sloped seabed. In: International Conference on Offshore Mechanics and Arctic Engineering, Vol. 47462. pp. 339–347.

Cadell, W., 2002. Report on the generation and analysis of DEMs for spatial modelling. https://macaulay.webarchive.hutton.ac.uk/LADSS/documents/DEMs-for-spatial-modelling.pdf. (Accessed 21 May 2024).

Chen, Y., Ding, Y., Hu, Z.Z., Ren, Z., 2025. Geometrized task scheduling and adaptive resource allocation for large-scale edge computing in smart cities. IEEE Internet Things J.

Chen, M., Yuan, G., Li, B., Li, C., Ouyang, M., Li, L., Shi, W., Han, Z., Zhang, W., Chen, Z., 2024. Dynamic analysis of lift-off operation of offshore wind turbine jacket foundation from the transportation barge. Ocean Eng. 301, 117443.

China Classification Society, 2011. Guidelines for towage at sea. https://www.ccs.org.cn. (Accessed 15 May 2024).

- Cummins, W.E., 1962. The impulse response function and ship motion. In: Report 1661, Department of the Navy, David W. Taylor Model Basin, Hydromechanics Laboratory, Research and Development Report, October 1962.
- Deng, J., Liu, S., Xie, C., Liu, K., 2021. Risk coupling characteristics of maritime accidents in Chinese inland and coastal waters based on NK model. J. Mar. Sci. Eng. 10 (1), 4.
- Deng, W., Wang, J., Guo, A., Zhao, H., 2024. Quantum differential evolutionary algorithm with quantum-adaptive mutation strategy and population state evaluation framework for high-dimensional problems. Inform. Sci. 120787.
- FCC, 2013. FCC begins shipping of the first large components for Açu Port by sea from algeciras to Brazil. https://www.fcc.es/en/. (Accessed 21 May 2024).
- Feng, A., Chen, K., You, Y., Jiang, S., 2021. Three dimensional numerical modelling for wave radiation problem under arbitrary seabed condition. Ocean Eng. 230, 108885.
- Feng, A., You, Y., Cai, H., 2019. An improved Rankine source panel method for three dimensional water wave problems. Int. J. Nav. Archit. Ocean. Eng. 11 (1), 70–81.
- Ferreira, M.D., Newman, J.N., 2009. Diffraction effects and ship motions on an artificial seabed. In: Proceedings of the 24th International Workshop on Water Waves and Floating Bodies. pp. 19–22.
- Gu, H., Xu, Q., Wang, H., Feng, W., 2024a. Numerical analysis of dynamic response in large caissons during wet-towing after cable breakage. Water 16 (10), 1335.
- Gu, J., Zhang, Y., Chen, S., Sui, Y., Li, L., 2024b. Influence of freshwater on the vertical structure of tidal currents: A case study of the Pearl River Estuary. Estuar. Coast. Shelf Sci. 307, 108919.
- Hendry, R.W., 1983. Construction sequence modelling for harbour breakwater. Proc. Coast. Eng. Conf. 2, 1765–1785.
- Heo, J.K., Park, C.W., 2016. Time domain analysis on deck wetness of a caisson wet-towed in irregular waves. J. Korean Soc. Coast. Ocean. Eng. 28 (1), 27–33.
- Hosking, J.R.M., Wallis, J.R., 1997. Regional Frequency Analysis.
- Jiang, Z., Gao, Z., Ren, Z., Li, Y., Duan, L., 2018. A parametric study on the final blade installation process for monopile wind turbines under rough environmental conditions. Eng. Struct. 172, 1042–1056.
- Kang, H.Y., Kim, M.H., 2014. Safety assessment of caisson transport on a floating dock by frequency- and time-domain calculations. Ocean. Syst. Eng. 4 (2), 99–115.
- Li, S.W., Hu, Z.Z., Tse, Kam Tim, Weerasuriya, Asiri Umenga, 2016. Wind direction field under the influence of topography: part II: CFD investigations. Wind. Struct. 22 (4), 477–501.
- Liu, X., Miao, Q., Wang, X., Xu, S., Fan, H., 2021. A novel numerical method for the hydrodynamic analysis of floating bodies over a sloping bottom. J. Mar. Sci. Technol. 1–19.
- Liu, Y., Zhang, J.M., Min, Y.T., Yu, Y., Lin, C., Hu, Z.Z., 2023. A digital twinbased framework for simulation and monitoring analysis of floating wind turbine structures. Ocean Eng. 283, 115009.
- Ma, C., Zhang, T., Jiang, Z., Ren, Z., 2025. Dynamic analysis of lowering operations during floating offshore wind turbine assembly mating. Renew. Energy 122528.
- Magkouris, A., Belibassakis, K., Rusu, E., 2021. Hydrodynamic analysis of twin-hull structures supporting floating PV systems in offshore and coastal regions. Energies 14 (18), 5979.
- Nan, R., Li, D., Jin, C., Wang, Q., Zhu, L., Zhu, W., Zhang, H., Yue, Y., Qian, L., 2011. The five-hundred-meter aperture spherical radio telescope (FAST) project. Internat. J. Modern Phys. D 20 (06), 989–1024.
- National Transportation Safety Board Marine Accident Brief, 2013. Grounding of commercial towing vessel justice. https://www.ntsb.gov/investigations/AccidentReports/Reports/MAB1410.pdf. (Accessed 15 May 2024).

- ten Oever, E., Muilwijk, M., Muttray, M., 2014. A practical approach to shallow water mooring with varying seabed. Coast. Eng. Proc. (34), 76.
- Park, C.W., Seo, J.H., Shin, H.R., 2018. Model tests of a caisson in wet towing for assessing resistance and stability in calm water and waves. J. Offshore Mech. Arct. Eng. 140 (5), 051301.
- Pilatis, A.N, Pagonis, D.N., Serris, M., Peppa, S., Kaltsas, G., 2024. A statistical analysis of ship accidents (1990–2020) focusing on collision, grounding, hull failure, and resulting hull damage. J. Mar. Sci. Eng. 12 (1), 122.
- Qiu, F., Wei, K., Xiang, Q., Jiang, Z., 2023. Effects of local scour and caisson geometry on the drag force of bridge foundations under steady flow. Appl. Ocean Res. 133, 103506
- Recommended ITTC, 2011. Procedures and Guidelines: Practical Guidelines for Ship CFD Applications, 7.5. ITTC, Boulder, CO, USA.
- Ren, Z., Verma, A.S., Ataei, B., Halse, K.H., Hildre, H.P., 2021. Model-free anti-swing control of complex-shaped payload with offshore floating cranes and a large number of lift wires. Ocean Eng. 228, 108868.
- Sun, M., Wang, S., Han, G., Jin, G., Li, J., Chen, H., Sun, Y., 2023. Multi-cable antiswing system for cranes subject to ship excitation and wind disturbance: Dynamic analysis and application in engineering. Ocean Eng. 281, 114518.
- Takagi, K., Naito, S., Hirota, K., 1994. Hydrodynamic forces acting on a floating body in a harbor of arbitrary geometry. Int. Offshore Polar Eng. Conf. 4 (1), 315–326.
- Transportation Safety Board of Canada, 2008. Marine investigation report M08m0010. https://www.tsb.gc.ca/eng/rapports-reports/marine/2008/m08m0010/m08m0010. html. (Accessed 15 May 2024).
- Verma, A.S., Jiang, Z., Ren, Z., Gao, Z., Vedvik, N.P., 2020. Effects of wind-wave misalignment on a wind turbine blade mating process: Impact velocities, blade root damages and structural SafetyAssessment. J. Mar. Sci. Appl. 19, 218–233.
- Wang, S., Moan, T., Gao, Z., 0000. Time-domain fatigue analysis methodology for semi-submersible hulls of floating wind turbines, Available at SSRN 5080108.
- Wang, J., Ren, Y., Shi, W., Collu, M., Venugopal, V., Li, X., 2025. Multi-objective optimization design for a 15 MW semisubmersible floating offshore wind turbine using evolutionary algorithm. Appl. Energy 377, 124533.
- Wei, K., Qiu, F., Qin, S., 2022. Experimental and numerical investigation into effect of skirted caisson on local scour around the large-scale bridge foundation. Ocean Eng. 250, 111052.
- Xing, J., Chen, S., 2017. A process study of the interaction of tidal currents, tidal mixing and density gradients in a region of freshwater influence. J. Mar. Syst. 172, 51–63.
- Ye, J., Shan, J., Zhou, H., Yan, N., 2021. Numerical modelling of the wave interaction with revetment breakwater built on reclaimed coral reef islands in the South China sea—Experimental verification. Ocean Eng. 235, 109325.
- Zhang, T., Ren, Z., 2025. Restricted isometry property in wave buoy analogy and application to multispectral fusion. IEEE Trans. Intell. Transp. Syst..
- Zhang, X., Zhang, S., Lei, Y., Zheng, X., 2023. Design and seakeeping performance of a shallow-sea surface litter collection device. J. Phys. Conf. Ser. 2565 (1), 012013.
- Zhao, T., Sun, M., Wang, S., Han, G., Wang, H., Chen, H., Sun, Y., 2024. Dynamic analysis and robust control of ship-mounted crane with multi-cable anti-swing system. Ocean Eng. 291, 116376.
- Zhou, L., Sun, Q., Ding, S., Han, S., Wang, A., 2023. A machine-learning-based method for ship propulsion power prediction in ice. J. Mar. Sci. Eng. 11 (7), 1381.
- Zhou, H., Ye, J., 2022. Numerical study on the hydrodynamic performance of a revetment breakwater in the South China Sea: A case study. Ocean Eng. 256, 111497